Maria Sklodowska-Curie Actions (MSCA)
Innovative Training Networks (ITN)
H2020-MSCA-ITN-2018
Grant number 813137

Project number 813137

URBASIS-EU
New challenges for Urban Engineering Seismology

DELIVRABLE

Work Package: WP1
Number: D1.5 - Spatial variability of earthquake ground motion: insights from 3D physics-based numerical simulations.

Authors:	**Lin, Jiayue**	(POLIMI)
Co-Authors:	Smerzini, Chiara	(POLIMI)
	Infantino, Maria	(POLIMI formerly)

Reviewers	Wassermann, Joachim
Approval	Management Board
Status	Final Version
Dissemination level	Public
Delivery deadline	31.10.2020
Submission date	09.02.2021
Intranet path	https://urbasis-eu.osug.fr/Scientific-Reports-157

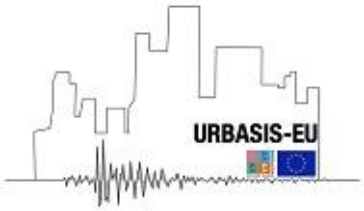

TABLE OF CONTENTS

1. Introduction

One of the key issues in the seismic risk assessment of spatially distributed portfolios of assets or infrastructural systems (e.g. lifelines), which are the backbone of an urban environment, is the modeling of the spatial correlation of ground motion intensity measures (IMs). Indeed, if during the same earthquake all structures of a portfolio can be affected, it is not correct to treat the IMs at all sites as independent variables, especially if they are located closely in space. As an example, Weatherill et al. (2015) considered the impact of spatial correlation on the aggregated loss analysis of synthetic building portfolios in the Tuscany region (Italy) and concluded that, on one side, considering spatial correlation produces greater losses at longer return periods, and, on the other side, that such an impact is sensitive to the spatial scale, type and degree of heterogeneity of the portfolio. Similar conclusions were drawn by Park et al. (2007) who demonstrated that, for large and small portfolios in San Francisco Bay Area in Northern California (see Figure 1.1), the underestimation of losses starts at values of annual mean rate of exceedance less than about 7×10^{-3} and 1×10^{-2} (i.e., at return periods larger than about 100-150 years) respectively, and maximum differences of almost a factor of 2 can be found for smaller portfolios at very large return periods (10^4 years). In a similar study, Goda and Atkinson (2009) showed that the inclusion of the correlation structure of ground motion parameters may have a remarkable impact on the estimated seismic losses by a factor as high as 50%. Recently, Garakaninezhad and Bastami (2019) investigated the issues related to the correlation of vertical ground motions and found that neglecting spatial correlation may provide unsafe evaluations of seismic performance of a bridge network.

These considerations led to the development of several spatial correlation models for different IMs, mainly in terms of Spectral Accelerations (SA) at different periods (T), using datasets of ground motion recordings (e.g., Wang and Takada, 2005; Jayaram and Baker, 2009; Goda and Hong, 2008; Goda and Atkinson, 2010; Sokolov et al., 2010; Esposito and Iervolino, 2011, 2012; Huang and Galasso, 2019). For a thorough overview of the existing empirical models, we refer the reader to the recent review published by Schiappapietra and Douglas (2020). However, it should be noted that the ground motion correlation structure depends strongly on local geologic conditions (region-specific) as well on source and path effects (scenario-specific), therefore a single generalized spatial correlation model may not be appropriate to represent specific regions, as pointed out by Sokolov et al. (2010) for the Taiwan case, and, more recently, by Schiappapietra and Douglas (2020) for Central Italy. Thus, the spatial correlation models proposed in literature, based on the analysis of wide strong motion datasets, may be not fully representative of the specific area under study.

A powerful tool which allows to obtain detailed and region-specific estimates of earthquake ground shaking and of its spatial variability is represented by 3D Physics-Based Numerical Simulations (3D PBS). The numerical simulations are based on physical models of the seismic source, the propagation path from the source to the site and local geologic irregularities. In this work, we used the 3D PBS generated by the Discontinuous Galerkin Spectral Element code SPEED (Mazzieri et al. 2013, http://speed.mox.polimi.it/), developed at Politecnico di Milano and already used in several case studies both for verification within international benchmarks, for validation with recorded near-source ground motion or for generation of future realistic earthquake ground motion scenarios (e.g. Smerzini et al. 2017; Paolucci et al. 2020; Infantino et al. 2020). To enrich the frequency content of PBS, limited typically to about 1.5-2 Hz, broadband ground motions have been generated by coupling SPEED results with an Artificial Neural Network (ANN) technique (Paolucci et al. 2018).

The advantages of a physics-based spatial correlation model are essentially two: (1) availability of thousands of receivers 'recording' the same (simulated) earthquake; (2) inclusion of the physics of the earthquake, from

the source up to the site. It follows that PBSs allow for a careful investigation of the dependence of spatial correlation on physical factors, such as magnitude, wave propagation effects, local site conditions, for a variety of "virtual", *albeit* realistic, conditions. A similar study has been done by Chen and Baker (2019), who developed spatial correlation maps for different earthquake scenarios and for different reference sites in the Los Angeles region.

With this premise, this report presents the research activities carried out by the ESR 1.3 (Politecnico di Milano) in the framework of the Work Package 1 (*WP1 – Low Probability/High Consequences Earthquakes*), focused on the quantification of spatial correlation from 3D PBSs. The goal of the work is, first, to verify the accuracy of the synthetics to reproduce a realistic spatial correlation of ground motion, as inferred from the analysis of strong motion recordings, and, second, to investigate systematically the influence of different physical factors, such as magnitude, source directivity, source-to-site path.

Geostatistical tools, based on the computation of both semivariograms and Pearson's correlation coefficient, are used to estimate the correlation of SA(T) across space for different horizontal components. The numerical dataset encompasses different areas worldwide (Po Plain, L'Aquila, Marsica, Sulmona, Norcia, in Italy; Istanbul, in Turkey; Thessaloniki, in Greece) and moderate to severe earthquake scenarios (M=6-7+) in near-source conditions.

The report is organized as follows. Section 2 illustrates the simulation dataset (numerical approach and case studies considered), while Section 3 explains the geostatistical method adopted for the evaluation of spatial correlation (semivariogram and Pearson's correlation coefficient). In Section 4, after some sensitivity analyses on the geostatistical tool (e.g. number of receivers; choice of median regression for computing the intra-event residuals), an overview of the main results derived from the PBS dataset is presented. In Section 5 the dependence of spatial correlation, i.e. correlation length (range) and variance (sill), on magnitude, ground motion component, source-to-site path is explored and discussed. Finally, in Section 6, spatial correlation is analyzed relaxing the hypotheses of isotropy and stationarity and maps of the Pearson's correlation coefficient are shown for a suite of earthquake scenarios in the Istanbul area.

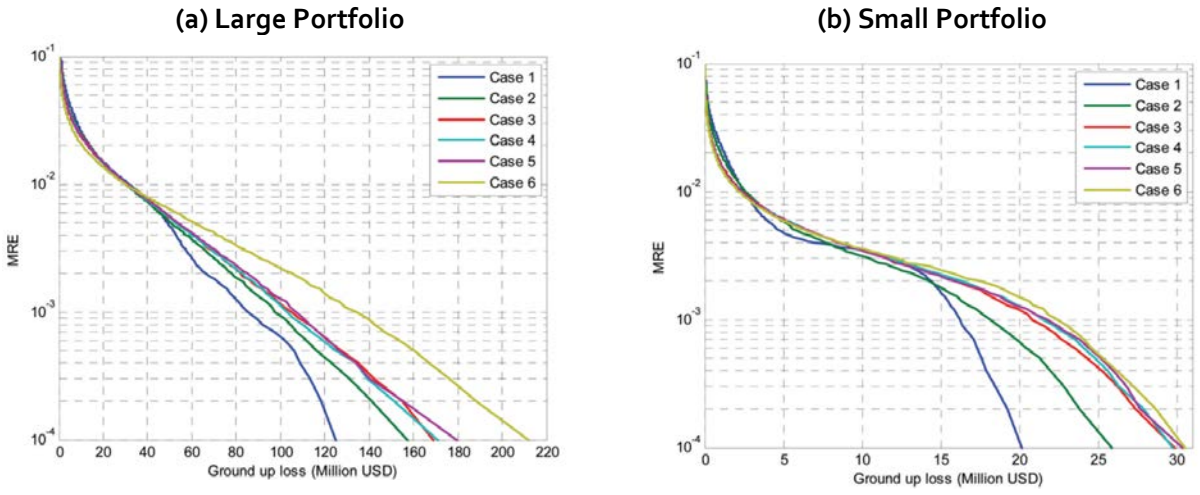

Figure 1.1 Mean Rate of Exceedance (MRE) curves for losses to a large (a) and small portfolio (b) computed using six different correlation models: (1) no correlation, (2)-(3)-(4)-(5) spatially correlated ground motion field according to different models and (6) perfect correlation. Adapted from Park et al. (2007).

2. Broadband Physics-Based numerical Simulations (PBS) of earthquake ground shaking scenarios

This section aims at describing the simulation method adopted to generate the dataset of broadband PBS ground motions considered in this study. For each PBS, the whole procedure adopted can be summarized in the following steps:

- Setup of the 3D numerical model: collection of the input data, construction of the 3D geological model, definition of the source model, execution of the numerical simulation by SPEED;
- ANN2BB: generation of broadband ground motions from 3D PBSs through an Artificial Neural Network technique.

2.1 Setup of the 3D numerical model

Once that the topographical, geotechnical and geological information are collected, the 3D geological model can be constructed combining: (a) the digital elevation model; (b) the crustal structure generally described in form of a layered model of S and P wave velocity (V_S and V_P), and (c) the local shallow geological structure with a model of V_S and V_P variable both in the horizontal and vertical direction, and possibly including the corresponding models for internal soil damping and non-linear curves (variation of shear modulus and damping ratio as a function of shear strain). Such a model is then combined with that of the source based on seismo-tectonic knowledge. For the case studies discussed in the present work, a kinematic rupture generator has been used applying along the fault a heterogeneous slip distribution combined with a slip source function, typically a sigmoid one, with initiation time and length depending on the local rupture velocity and rise-time. Note that in SPEED two kinematic rupture generators are available, namely, Herrero and Bernard (1994) and Schmedes et al. (2012), referred to in the sequel as HB94 and SEA12. The source and velocity models obtained are then condensed into a spectral element numerical model consisting of hexahedral elements with a spectral degree selected in order to propagate a maximum reliable frequency typically of about 1.5-2 Hz.

2.2 ANN2BB: generation of broadband ground motions

A fundamental step of SPEED post-processing concerns the generation of broadband ground motions, where the low-frequency simulated waveforms are enriched in the high-frequency range to produce time histories with a realistically broad frequency content. This is an essential step to make synthetics usable for earthquake engineering applications, such as risk analyses. In this study, broadband ground motions have been obtained through an approach based on Artificial Neural Network (ANN), referred to as ANN2BB, presented and validated against real case studies in Paolucci et al. (2018). While we refer the reader to the relevant publication for a detailed description of the methodology, we limit herein to recall the main features of the approach. In the ANN2BB approach, an ANN is trained based on a dataset of strong motion records to predict short period spectral ordinates ($T<T^*$) based on long period ones ($T\geq T^*$), being T^* the minimum period of the numerical model. The recording dataset may be selected by the user among the ones available in the literature, such as SIMBAD (Smerzini et al. 2014) or NGA-West 2 (Ancheta et al. 2013). Then, for each simulated receiver, a target ANN2BB response spectrum is computed (see Figure 2.1), the spectral ordinates of which, for $T\geq T^*$, coincide with the simulated ones, while, for $T<T^*$, they are obtained from the ANN (median value over 20 ANN realizations, separately for horizontal and vertical components).

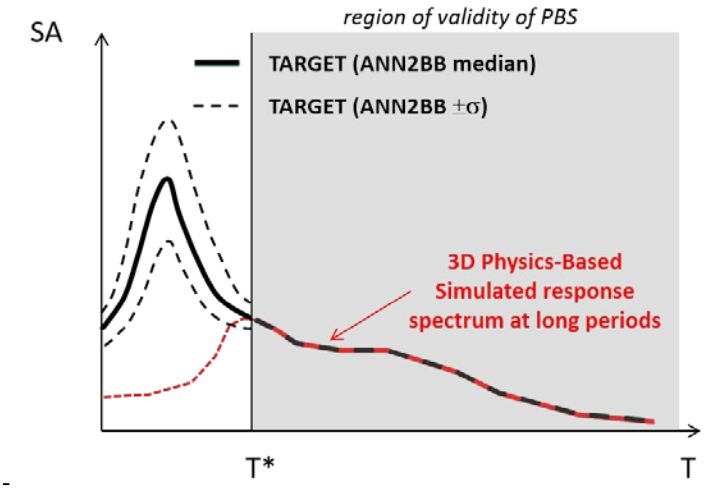

Figure 2.1 Construction of the target broadband spectrum using the ANN2BB approach.

2.3 Overview of PBS dataset

An overview of the PBS dataset considered in this work for the evaluation of spatial correlation is given in Table 2.1. The PBS dataset includes 7 different regions worldwide (namely, L'Aquila, Sulmona, Po Plain, Marsica and Norcia, in Italy; Thessaloniki in Greece and Istanbul in Turkey) and rupture scenarios with magnitude in the range M_W=6-7.4. The geological conditions are also rather variable, passing from regions with very soft soil basins (e.g. Marsica) to regions with stiff and small basins (e.g. Norcia). It is worth recalling that the PBS included in this dataset were already verified and validated in previous projects.

A total of 19 scenarios were used to computed the semivariogram (see Figure 2.2), while, referring to the Istanbul case study, further 31 scenarios were considered to calculate the Pearson's correlation coefficient (see Section 6).

The data of ground motion scenarios are accessible at the following web-repository: http://speed.mox.polimi.it/WebRepository/[1].

[1] Some scenarios will be available soon.

Table 2.1 List of PBSs computed by SPEED and considered in this work.

Region	Fault	Style of Faulting	Model size (km³)	$V_s^{surface}$ (m/s)	Moment Magnitude M_W	No. Scenarios	References
L'Aquila, Central Italy	Paganica	Normal	58x58x20	300-1700	6.2	1	Evangelista et al. (2017)
Sulmona, Central Italy	Mt. Morrone	Normal	49x42x13	500-1200	6.0	5	Villani et al. (2014)
					6.5	3	
Po Plain, Northern Italy	Mirandola	Reverse	74x51x20	300	6.0	1	Paolucci et al. (2015)
Marsica, Central Italy	Fucino	Normal	56x46x20	100-1000	6.7	1	Paolucci et al. (2016)
Norcia, Central Italy	Norcia	Normal	50x40x21	280-1700	6.5	1	Ozcebe et al. (2019)
Istanbul, Turkey	North Anatolian Fault (Marmara Sea)	Strike-Slip	165x100x30	250-1350	7.0	4 + 11*	Infantino et al. (2020)
					7.4	1 + 20*	
Thessaloniki, Northern Greece	Gerakarou	Normal	82x64x31	300-2000	6.5	1	Smerzini et al. (2017); Smerzini et al. (2018)
	Anthemountas	Normal			7.0	1	

**scenarios used to compute the Pearson's coefficient*

Po Plain - *Northern Italy*

Scen ID	HYPO(Lon(E°),Lat(N°),Depth(km))	Mw
1-PPL	11.072, 44.8501, 10.7	6.0

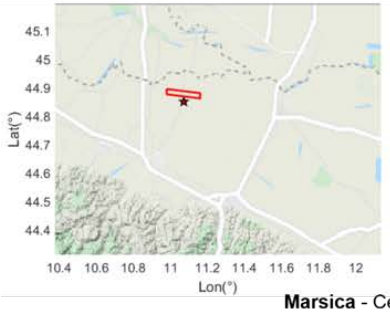

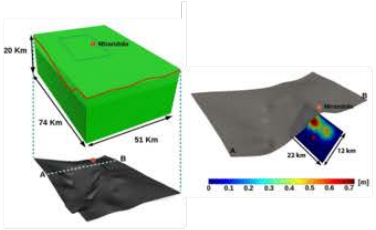

Marsica - Central *Italy*

Scen ID	HYPO(Lon(E°),Lat(N°),Depth(km))	Mw
1-MAR	13.6066, 41.9738, 6.4	6.7

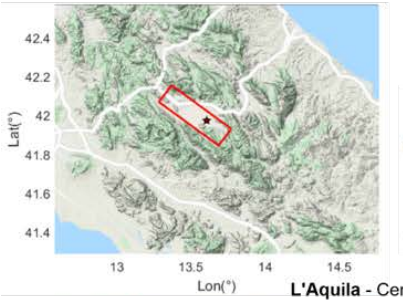

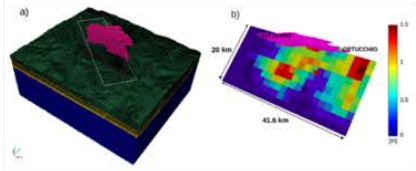

L'Aquila - Central *Italy*

Scen ID	HYPO(Lon(E°),Lat(N°),Depth(km))	Mw
1-AQU	13.3721, 42.3562, 9.037	6.2

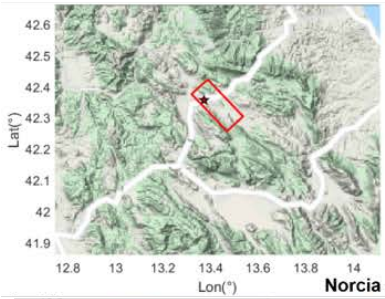

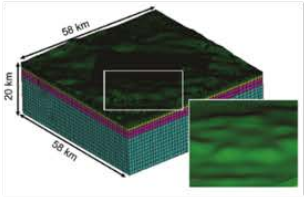

Norcia - *Italy*

Scen ID	HYPO(Lon(E°),Lat(N°),Depth(km))	Mw
1-NOR	13.1152, 42.8494, 6.3	6.5

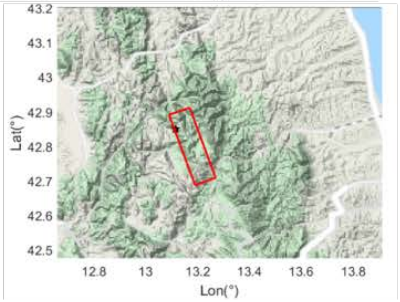

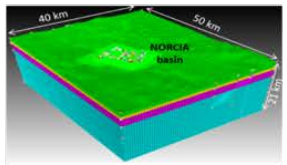

Thessaloniki - *Northern Greece*

Scen ID	HYPO(Lon(E°),Lat(N°),Depth(km))	Mw
1-THE	23.266, 40.705, 7.4	6.5
2-THE	23.1411, 40.5173, 9.5	7.0

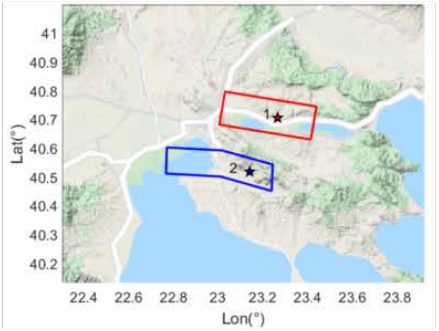

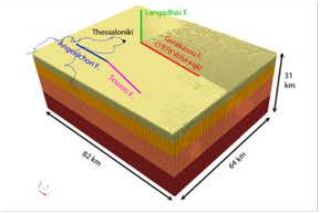

Sulmona - *Central Italy*

Scen ID	HYPO(Lon(E°),Lat(N°),Depth(km))	Mw
1-SUL	13.8301, 42.1145, 6.1	6.0
2-SUL	13.8674, 42.0785, 7.3	6.0
3-SUL	13.8348, 42.1084, 6.4	6.0
4-SUL	13.8121, 42.1130, 8.1	6.0
5-SUL	13.8450, 42.1001, 6.6	6.0
6-SUL	13.8970, 42.0624, 6.561	6.5
7-SUL	13.8641, 42.0753, 8.0688	6.5
8-SUL	13.8400, 42.1091, 5.8110	6.5

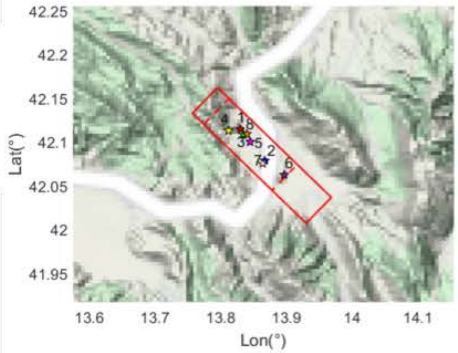

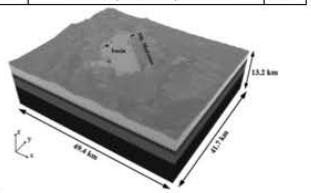

Istanbul - *Turkey*

Scen ID	HYPO(Lon(E°),Lat(N°),Depth(km))	Mw
1-IST	28.4597, 40.8458, 7.4	7.0
2-IST	28.3356, 40.8332, 10.4	7.0
3-IST	28.6619, 40.8660, 8.5	7.0
4-IST	28.4679, 40.8466, 10.0	7.0
5-IST	28.6707, 40.8640, 9.4	7.4

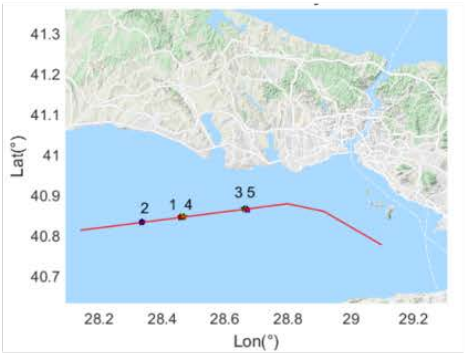

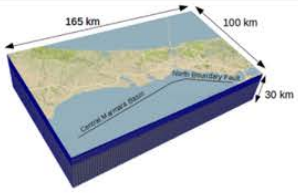

Figure 2.2 Overview of case studies of 3D PBS in large urban areas worldwide for semivariogram calculation.

3. Geostatistical tools

This section briefly introduces the geostatistical tools commonly used in seismology and in other fields to describe the spatial correlation of a random function (Zimmerman and Stein, 2010).

3.1 Basic definitions: the semivariogram

Let us consider a spatially distributed random function $Z(\boldsymbol{x}) = (Z_{x1}, Z_{x2}, \ldots, Z_{xi}, \ldots, Z_{xn})$, where Z_{xi} is the random variable considered at the site i located at the place x_i. Random variables are spatially correlated at some scale and it can be quantified by means of the semivariogram γ, a geostatistical tool that describes the average dissimilarity of two random variables as follows:

$$\left(Z_{xi}, Z_{xj}\right) = \frac{1}{2} Var\left(Z_{xi} - Z_{xj}\right) = \frac{1}{2} E\left[\left\{Z_{xi} - Z_{xj}\right\}^2\right] \quad (1)$$

where *Var* and *E* denote the variance and expected value, respectively. Residuals of ground motion intensity measures within a set of sites for a given earthquake are regarded as spatial random variables. For each site, however, we do not have multiple realizations of a given earthquake, making it impossible to draw inferences from it. Consequently, to overcome this limitation, the random function $Z(\boldsymbol{x})$ is assumed a second-order (or weaker) stationary process, which implies that: (i) the expected value of the random variable Z_x is constant across space: $E(Z_x) = \mu$, where μ is constant; (ii) the covariance depends only on the separation distance vector **h**: $C(\boldsymbol{h}) = cov(Z_x, Z_{x+h})$, where $C(\boldsymbol{h})$ is independent of x.

With the second-order stationary assumption, the semivariogram depends only on the separation vector **h** and covariance and semivariogram are equivalent:

$$\gamma(\boldsymbol{h}) = \frac{1}{2} Var(Z_x - Z_{x+\boldsymbol{h}}) = \frac{1}{2} E[\{Z_x - Z_{x+\boldsymbol{h}}\}^2] \quad (2)$$

$$\gamma(\boldsymbol{h}) = C(\boldsymbol{0}) - C(\boldsymbol{h}) = \sigma^2 - C(\boldsymbol{h}) \quad (3)$$

where $C(\boldsymbol{0}) = \sigma^2$ is the variance of Z_x. Moreover, we can introduce the spatial correlation coefficient defined as:

$$\rho(\boldsymbol{h}) = \frac{C(\boldsymbol{h})}{\sigma^2} = 1 - \frac{\gamma(\boldsymbol{h})}{\sigma^2} \quad (4)$$

Modeling the spatial correlation with semivariograms is generally carried out by the following steps: (1) calculation of the sample semivariogram $\hat{\gamma}(\boldsymbol{h})$ from the data set; (2) selection of the proper theoretical semivariogram model fitting the data; (3) estimation of the parameters for the chosen model.

Referring to the first point, the sample semivariogram is estimated through the method of moments (Matheron 1965):

$$\hat{\gamma}(\boldsymbol{h}) = \frac{1}{2N(\boldsymbol{h})} \sum_{j=1}^{N(\boldsymbol{h})} \{z_{x_j} - z_{x_j+\boldsymbol{h}}\}^2 \quad (5)$$

where $z_{x_j} - z_{x_j+\boldsymbol{h}}$ is the difference between the data at sites separated by $\boldsymbol{h}$ and $N(\boldsymbol{h})$ denotes the total numbers of pairs at lag $\boldsymbol{h}$. It is worth mentioning that the sample semivariogram can be computed using the more robust estimator proposed by Cressie and Hawkins (1980), less sensitive to the outliers. Once that sample semivariogram is computed, a functional form (negative definite) fitting the data has to be selected. The basic models generally used to this end are the Exponential, Gaussian or Spherical models (see Figure 3.1). The exponential model, used in this work, is defined for an isotropic case (i.e., the vector distance $\boldsymbol{h}$ is replaced by a scalar h) by the following equation:

$$\gamma(h) = a\left[1 - \exp\left(-\frac{3h}{b}\right)\right] \quad (6)$$

The parameters *a* and *b* of Equation (6) are called *sill* and *range*, and represent the variance of the random process and the separation distance at which the data can be considered fully uncorrelated, respectively.

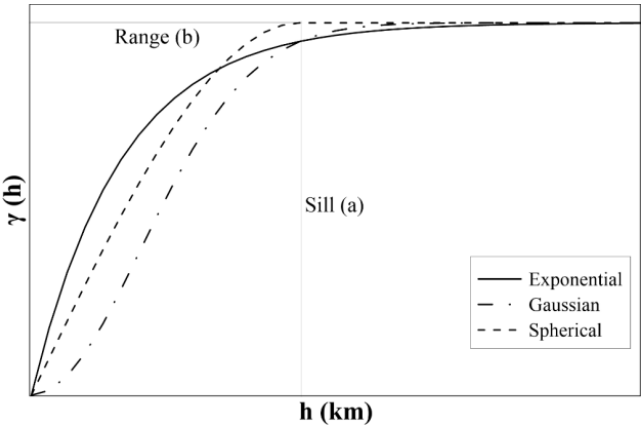

Figure 3.1 Semivariogram models: exponential, gaussian and spherical. Definition of range and sill parameters.

3.2 Application to earthquake ground motions

The procedure introduced in the previous section allows to estimate the theoretical semivariogram, $\gamma(\boldsymbol{h})$, under the assumption of a full random process. The latter is the superposition of two contributions, the mean μ (assumed to be constant) and $\varepsilon(\boldsymbol{x})$ is a random variable of zero mean and covariance $C(\boldsymbol{h})$. If the random process has a trend, such as in the case of ground motion intensities which attenuate with distance, μ varies in a predictable manner depending on the position ($\boldsymbol{x}$), see Equation (7), and the semivariogram has to be computed using the residuals $\varepsilon(\boldsymbol{x})$ with respect to the median prediction of a ground motion model (i.e., replacing $Z_x - Z_{x+\boldsymbol{h}}$ with $\varepsilon_x - \varepsilon_{x+\boldsymbol{h}}$ in Equation (2) and (5)).

$$Z(\boldsymbol{x}) = \mu(\boldsymbol{x}) + \varepsilon(\boldsymbol{x}) \tag{7}$$

Ground motion models predict intensities at a site *s* due to an earthquake *e* and take the general form:

$$log_{10}\, Y_{se} = log_{10}\, \bar{Y}_{se}(M, R, S, \delta) + \eta_e + \varepsilon_{se} \tag{8}$$

where Y_{se} denotes the IM of interest, e.g. SA(T); $\bar{Y}_{se}$ is the predicted median value as a function of magnitude (M), source-to-site distance (R), local-site conditions (S) and others parameters (δ); η_e is the inter-event residual, which is a random variable with zero mean constant during the same earthquake across all the sites, and ε_{se} represents the intra-event residuals, a random variable with zero mean variable site-to-site.

Thus, the spatial correlation is computed on the intra-event residuals ε_{se} as the logarithmic (log_{10}) misfit between the simulated $SA(T)$, Y_{se}, at the site $\boldsymbol{x}$ with respect to a median trend $\bar{Y}_{se}$ given by the following relationship:

$$log_{10}\bar{Y}_{se} = c_1 - c_2 log_{10}(R_{line} + c_3) + c_4 log_{10}\left(\frac{V_{S30}}{800}\right) \tag{9a}$$

$$log_{10}\bar{Y}_{se} = c_1 - c_2 log_{10}(R_{line} + c_3) + c_4 H_{bed} \tag{9b}$$

where c_i, with i=1,...4, are the model coefficients calibrated by Least-Squares (LS) regression, R_{line} is the closest distance from the surface fault projection of the segment at the top edge of the rupture plan (see definition in Paolucci et al. 2016), V_{S30} is the time-averaged shear wave velocity in the top 30 meters and H_{bed} is the depth of the alluvial-bedrock interface. Equation (9b) is adopted for the Po plain case study, since the corresponding numerical model is characterized by a highly irregular bedrock interface with a homogeneous

distribution of V_{S30} at all sites of the model. As regards the distance metric, R_{line} is used instead of more standard metrics, such as R_{JB} and R_{rup}, because studies underway suggest that it is more efficient (i.e. lower dispersion) in near-source conditions.

Note that, at variance with most works where the spatial correlation is estimated on the intra-event residuals with respect to the median predictions of existing empirical ground motion models (e.g. Jayaram and Baker 2009, Esposito and Iervolino 2011, 2012), in this work, the regression of Equation (9) is calibrated on the specific dataset associated to each PBS.

From an operational point of view, the procedure to compute semivariograms from broadband PBSs belongs to the multistage class of approaches (Jayaram and Baker, 2010) and can be summarized as follows: (i) compute the intra-event residuals on SA at periods T=0,0.2, 0.5, 1, 2 and 3 s, $\varepsilon_{se} = log\, SA_{se} - log\, \overline{SA}_{se}$, separately for the horizontal components, i.e., Fault Normal (FN), Fault Parallel (FP) and geometric mean (GMH); (ii) divide the separation distance, h, in bins of constant width δ (iii) compute the sample semivariogram by the method of moments; (iv) fit the sample semivariogram by weighted LS regression using the exponential theoretical model and, hence, estimate the range and sill parameters.

In the procedure above, the exponential model is used for most of the cases because it is the model providing the best performance in terms of mean square error (MSE), with the exception of Istanbul, for which a spherical model is preferred because of the larger fit with the sample semivariogram. As regards the LS fitting, either a classical or weighted regression, with higher weights for short separation distances, was selected based on the minimum MSE. A bin width δ=2 km was chosen so that there is a stable trend of correlation with at least 30 pairs per bin (Journel and Huijbregts, 1978). Further details on the sensitivity analyses performed on the geostatistical analysis (median regression, type of LS fitting) are given in Section 4.1.

As opposed to the multistage approach, more recently, Ming et al. (2019) proposed a novel approach called one-stage scoring algorithm, where the ground motion model parameters and the spatial correlation parameters are both estimated in a single stage without introducing the semivariogram. The estimators produced by the one-stage scoring approach have good statistical properties (consistency, statistical efficiency, and asymptotic normality) and produce smaller prediction errors than the multistage algorithm. Furthermore, multi-stage approaches are only capable of estimations of isotropic and stationary correlation structures.

3.3 Pearson's correlation coefficient

The Pearson's correlation coefficient ρ is a statistical measure of the linear correlation between two variables X and Y. It ranges from –1 to +1: (i) a positive ρ implies that the two variables are positive correlated (i.e., if X increases, Y increases and vice versa, see Figure 3.2 a); (ii) a negative ρ implies that the two variables are negative correlated (i.e. if X increases, Y decreases and vice versa, see Figure 3.2 b); (iii) ρ =+ 1 indicates a perfect positive correlation (see Figure 3.2 c); (iv) ρ =-1 a total negative correlation (see Figure 3.2 d); (v) ρ =0 denotes two variables which are fully uncorrelated (Figure 3.2 e).

When computed from a sample, the Pearson's correlation coefficient can be estimated as follows:

$$\hat{\rho}(x,y) = \frac{\sum_{i=1}^{n}(x_i-\bar{x})(y_i-\bar{y})}{\sqrt{\sum_{i=1}^{n}(x_i-\bar{x})^2}\sqrt{\sum_{i=1}^{n}(y_i-\bar{y})^2}} = \frac{\sum_{i=1}^{n} z_{i,x}\cdot z_{i,y}}{\sqrt{\sum_{i=1}^{n} z_{i,x}{}^2}\sqrt{\sum_{i=1}^{n} z_{i,y}{}^2}} \quad (10)$$

where n is the sample size, x_i and y_i are the individual events in sample space, $\bar{x}$ and $\bar{y}$ are the sample means and $z_{i,x}$ and $z_{i,y}$ are the residuals of x_i and y_i with respect to the corresponding sample means (i.e. $z_{i,x} = x_i - \bar{x}$ and $z_{i,y} = y_i - \bar{y}$).

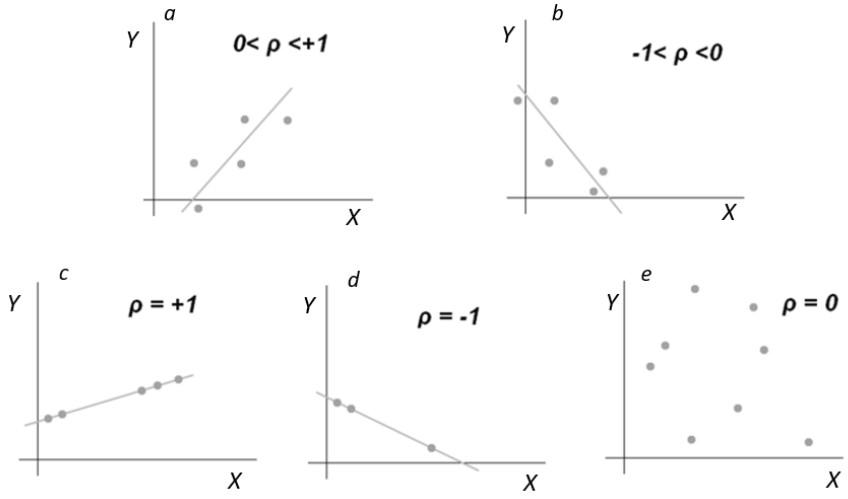

Figure 3.2 Examples of different Pearson's correlation coefficients ρ.

It follows that Equation (10) can be used to estimate the correlation coefficient of ground motion residuals between sites *j* and *k* as follows:

$$\hat{\rho}(x,y) = \frac{\sum_{i=1}^{n} z_{i,j} \cdot z_{i,k}}{\sqrt{\sum_{i=1}^{n} z_{i,j}{}^2} \sqrt{\sum_{i=1}^{n} z_{i,k}{}^2}} \tag{11}$$

where n is the number of rupture realizations of a given earthquake scenario (an earthquake scenario refers to a specified magnitude M, source-to-site distance and fault; instead, a rupture realization refers to a particular rupture scenario with prescribed hypocenter and slip distribution) and *z* is the intra-event residual estimated as:

$$z_{i,j} = \hat{\delta}W_{i,j} = \ln\left(IM_{i,j}\right) - \mathrm{m}_{\ln(IM_{i,j})} - \hat{\delta}B_i \tag{12}$$

where $\mathrm{m}_{\ln(IM_{i,j})}$ is the logarithmic mean of a given intensity measure, i.e., SA(T), and $\hat{\delta}B_i$ is the estimated between-event residual (defined as average misfit of ground motions of a particular event with respect to median prediction).

By setting IM=SA(T), $\mathrm{m}_{\ln(IM_{i,j})} = \mathrm{m}_{\ln(SA_{i,j})}$ is computed as sample mean of *ln(SA(T))* at site *j* over a suite of rupture realizations *i=1,…n* (note that the *n* earthquake realizations share the same magnitude and fault rupture extent). Considering the huge number m of stations available (of the order of thousands) for SPEED simulations, a reasonable estimate of the between-event residual is given by:

$$\hat{\delta}B_i = \frac{1}{m}\sum_{j=1}^{m}\left(\ln\left(SA_{i,j}\right) - \mathrm{m}_{\ln(SA_{i,j})}\right) \tag{13}$$

Differently from the semivariogram, which quantifies the correlation as a function of the inter-station separation distance, the Pearson's coefficient allows describing the correlation between any site *j* and *k* in a nonstationary and anisotropic fashion.

However, since such an approach requires observations of residuals $z_{i,x}$ and $z_{i,y}$ from multiple earthquake realizations, its applications has been limited due to the scarcity of recorded data. On the other hand, the numerousness of simulated ground motions allows using Pearson coefficient as a tool to investigate the

ground motion spatial correlation relaxing the hypotheses of stationarity and isotropy. Analysis of the Pearson's correlation coefficient for the CyberShake numerical simulations of the Los Angeles region has been recently addressed by Chen and Baker (2019).

4. Spatial correlation results

In this section, after discussing the results of some sensitivity analyses of the geostatistical tool, an overview of the most salient results obtained from different case studies is provided. For sake of completeness, in Appendix A, the complete set of results, for selected spectral accelerations, namely, PGA and SA(1s), and for both FN and FP components, are reported.

4.1 Sensitivity analyses

As a preliminary test, the effect of the functional form adopted for the estimation of the median trend, i.e., $log\,\overline{SA}_{se}$, is investigated to check the robustness of results. Specifically, four different functional forms were considered: (1) $c_1 - log_{10}(R_{line} + c_2)$; (2) $c_1 - c_2 log_{10}(R_{line})$; (3) $c_1 - c_2 log_{10}(R_{line} + c_3)$; (4) $c_1 - c_2 log_{10}(R_{line} + c_3) + c_4 H_{bed}$. Note that functions from (1) to (3) differs only in the geometric attenuation term, while (4) adds the site effect term. It is found that the calibration of a proper median function has a strong impact on the semivariogram trend and, hence, on the robustness of model parameters (range and sill). As a matter of fact, the differences of the grey and orange dots in Figure 4.1 indicate that the introduction of a two-coefficient geometric attenuation term allows one to get semivariogram with stable sill especially at long periods, without the need of applying de-trending techniques (Zimmerman and Stein, 2010). On the other hand, the introduction of the site term has a more limited effect and mostly at longer periods, as expected for the deep sites in the Po plain. These verifications, extended also to other case studies (not shown here for sake of brevity), confirmed that accuracy of the selected functional form (4), see Equation (9). Note also that for distances larger than around 60 km, a less representative sample of receivers is used in each bin (lower number and located at model boundaries) and, therefore, the semivariogram shows a decreasing trend with less robust estimates.

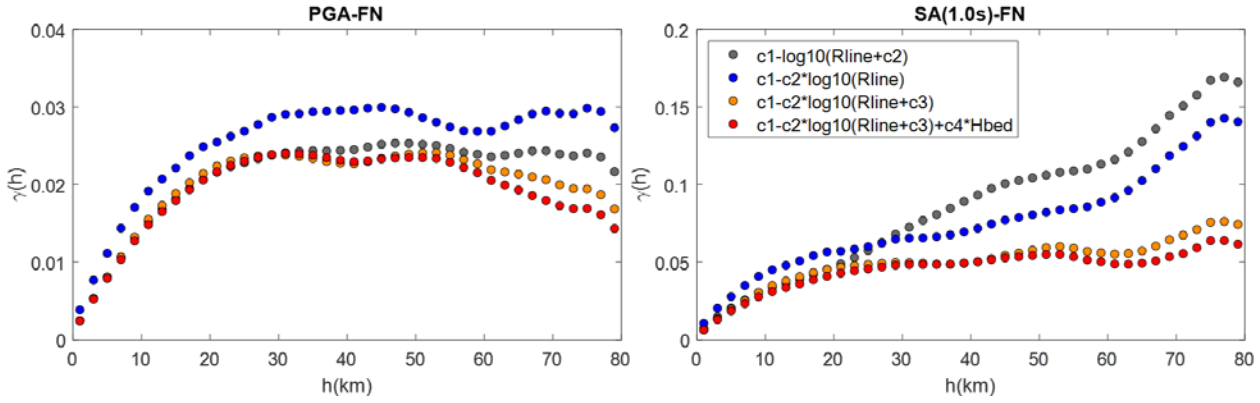

Figure 4.1 Effect of functional form for median trend in estimating the semivariogram: Po Plain, PGA-FN (left) and SA(1s)-FN (right).

Furthermore, the influence of the number of receivers in computing the semivariogram has been tested. It is well known that the most important factor determining the accuracy of the sample semivariogram is the number of data within each distance bin. In general, the accuracy increases with the number of data (Oliver and Webster,2014). With PBS, it is possible to check how the accuracy of the computed semivariogram varies with an increasing number of "numerical" receivers. To this end, for the Po plain case study and for PGA-FN and SA(1s)-FN, the semivariogram was computed as the average of 30 random realizations of sample of N receivers, with *N* = 10, 50, 100, 250, 500 and 1000, corresponding to an average spacing *s*= 18,

8, 5.5, 3.5, 2.5 and 1.8 km, respectively. In Figure 4.2 (left subplots), the dots and vertical bars indicate, for each distance bin, the average (μ) and ± standard deviation (σ) of the 30 samples. For clarity, the center and right subplots depict separately the μ and σ trends. These analyses point out that an average receiver spacing lower than 5.5 km approximately (N = 100) is needed to have accurate estimates with a stable mean and variance.

Note that in our analyses the complete set of numerical receivers, as provided by the fine spatial discretization of the numerical grid (with average inter-receiver distance of 500 m), was adopted, thus satisfying the above constraints on the maximum allowable spatial spacing.

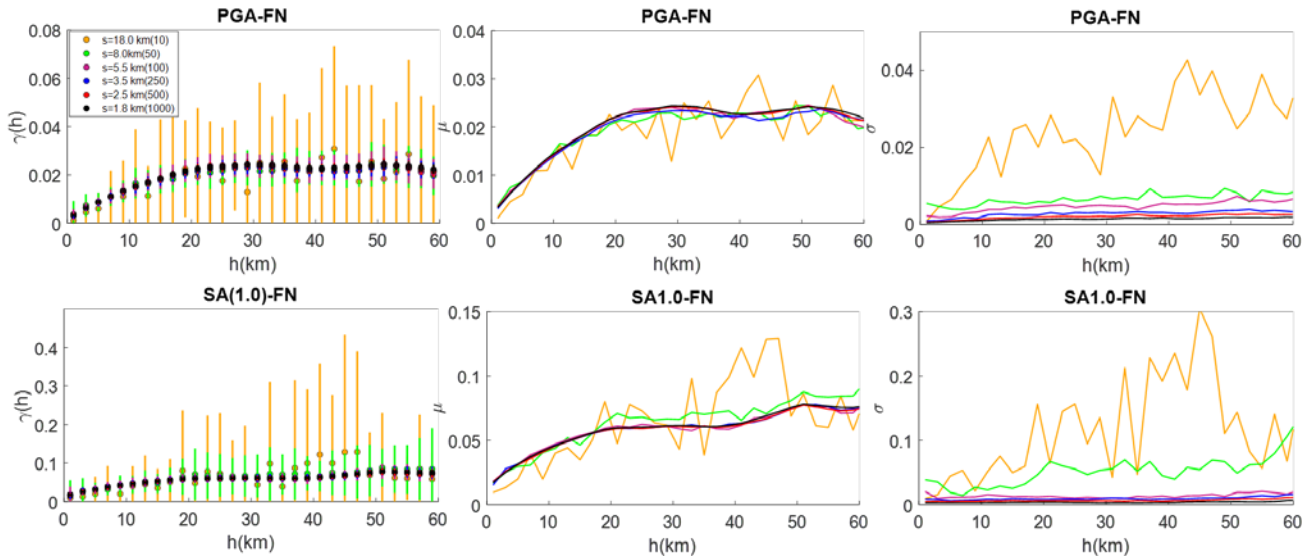

Figure 4.2 Influence of the number of receivers: Po Plain, PGA-FN (top) and SA(1s)-FN (bottom). Left: semivariogram (mean μ and ± standard deviation σ) for 30 random samples of N=10, 50, 100, 250, 500 and 1000 receivers with average spacing s=18, 8, 5.5, 3.5, 2.5 and 1.8 km, respectively; Center: μ(h); Right: σ(h).

After these tests, we show in Figure 4.3 and Figure 4.4 two illustrative examples of the multi-stage approach adopted in this study for the Po Plain case study and PGA-FN and SA(1.0s)-FN, respectively, in terms of: (a) map of log_{10} SA_{se}; (b) map of log_{10} $\overline{SA}_{se}$, with $\overline{SA}_{se}$ given by Equation (9b); (c) map of logarithmic residuals $\varepsilon_{se} = log_{10}\, Y_{se} - log_{10}\, \bar{Y}_{se}$; and (d) sample semivariogram (dots) and best-fitting exponential model.

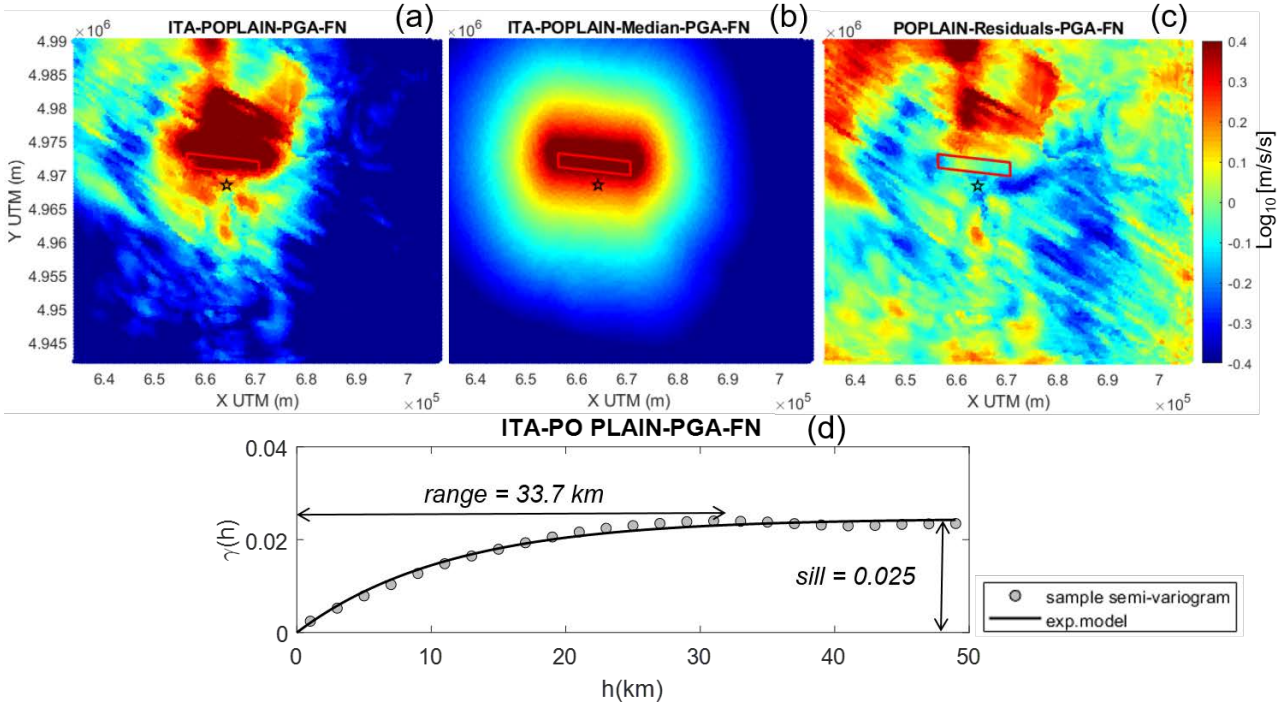

Figure 4.3 Illustrative example of the multi-stage approach adopted to compute the semivariogram: Po Plain, PGA-FN. (a) map of $log_{10} SA_{se}$; (b) map of median $log_{10} \overline{SA}_{se}$; (c) map of residuals $\varepsilon_{se} = log_{10} Y_{se} - log_{10} \overline{Y}_{se}$; (d) sample semivariogram (dots) and best-fitting exponential model obtained by LS regression.

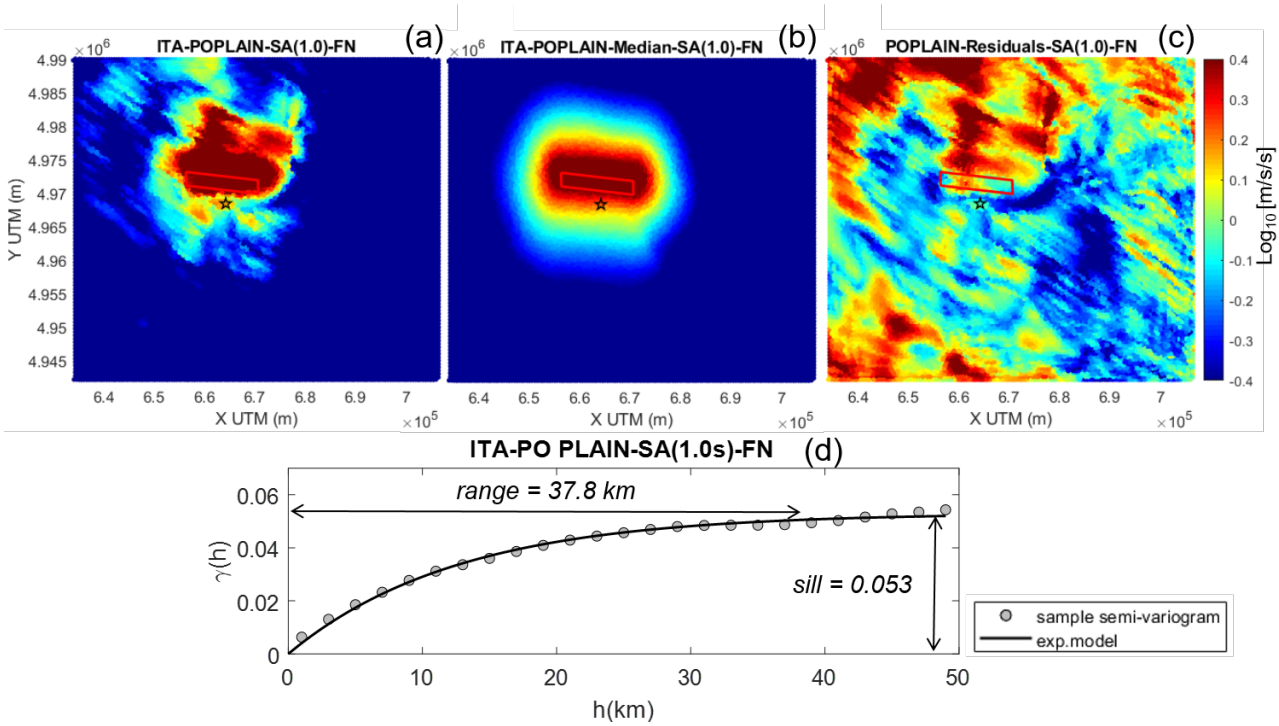

Figure 4.4 Same as in Figure 4.3 for SA(1.0s)-FN.

4.2 Overview of results and dependence on period

To provide an overview of the spatial correlation models calibrated on each PBS, Figure 4.5 and Figure 4.6 shows the range and sill as a function of period, respectively, for eight representative PBS. Specifically, for each case study and each causative fault (see Table 2.1), a single scenario has been considered (namely: M_W6.0 Po Plain – 29.05.2012, M_W 6.2 L'Aquila – 06.04.2009, M_W6.7 Marsica – 13.01.1915, M_W6.5 Norcia – 30.10.2016, M_W6.0 Sulmona, M_W6.5– 20.06.1978 and M_W7.0 Thessaloniki, M_W7.0 Istanbul) and the range/sill have been computed for six spectral ordinates: PGA, 0.2, 0.5, 1.0, 2.0 and 3.0 s.

The results are shown separately for the FN (filled symbols, continuous) and FP components (open symbols, dashed lines). When FN and FP components are not available (i.e. for segmented faults), the EW and NS components are considered. For the M6.0 Po plain case study (see top left panel of Figure 4.5 and Figure 4.6), our results are compared with the findings by Sgobba et al. (2019), who estimated the range and sill of the source-, site- and path- corrective terms of the ground motion model specific for the Po Plain region using a non-ergodic approach. Referring to the Po plain case, a good agreement is found with Sgobba et al. (2019) in terms of both sill and range (up to 1 s). As regards the range, the results by Sgobba et al. (2019) shows an abrupt increase of range at periods longer than 1 s up to values of about 130 km at T=4 s, while PBS-based estimates show that the range stabilizes between 30-40 km at long periods. Such discrepancies may be due to the different processing (residuals and number of data to compute the semivariograms) and to some unmodeled systematic site phenomena which are not fully captured by the residual decomposition in Sgobba et al. (2019).

The ranges estimated in this work generally increase with period, similarly to other literature studies (see Section 4.3 for a more detailed discussion on this point). This is consistent with past findings on spatial coherency of ground motion (e.g. Zerva and Zervas, 2002). Being a measure of the linear correlation between two waveforms at a given distance, spatial coherency decreases at increasing separation distance and at higher frequencies. In fact, high-frequency components are more affected by small-scale heterogeneities and therefore they turn out to be less coherent, compared to low-frequency waves (Kiureghian, 1996). Nevertheless, for some cases (e.g. ITA-EMI, GRC-THE-M6.5), it is found that the range is nearly constant or slightly decreasing for periods larger than around 1 s. A similar trend was also found in literature studies based on earthquake recordings, as further discussed in Section 4.3.

From the comparison of Figure 4.6 with Figure 4.5, it is clear that there is positive correlation between range and sill trend across all periods and, hence, a similar trend is found for the sill with increasing values for increasing periods. This trend is consistent with the behavior found by Sgobba et al. (2019) for the Po Plain region.

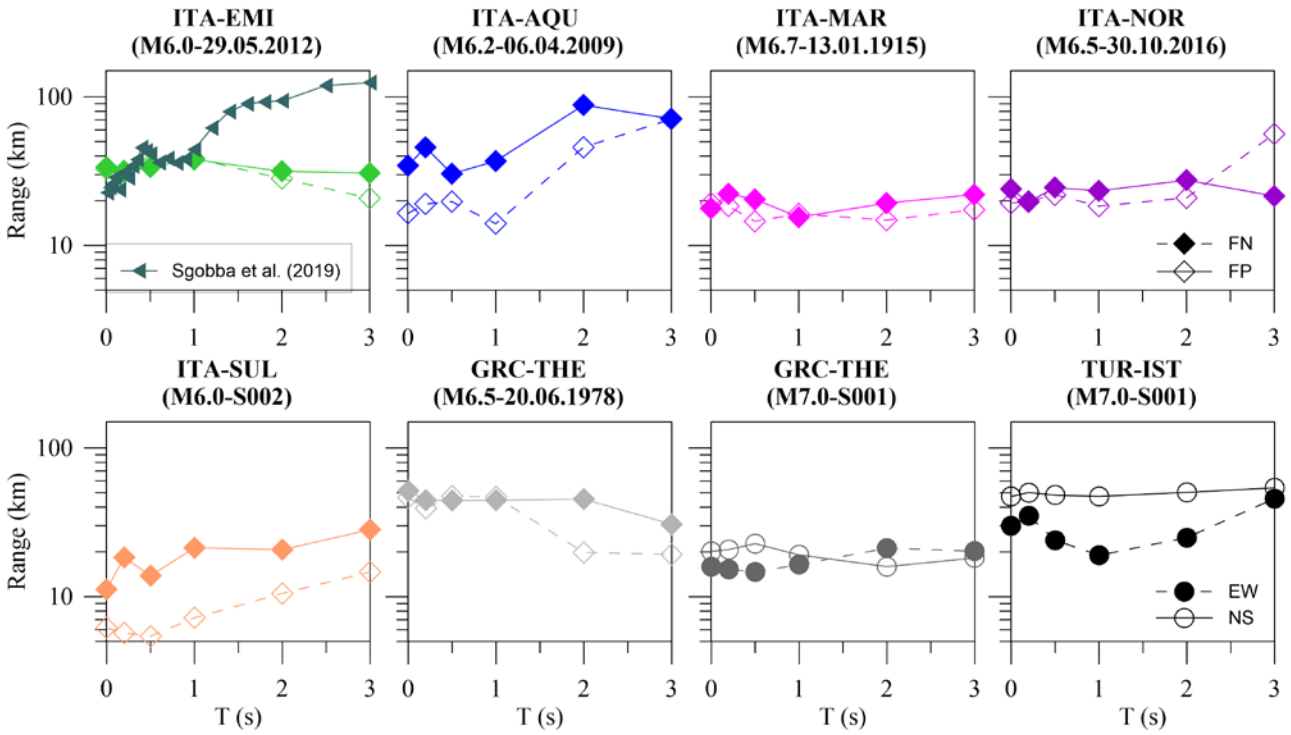

Figure 4.5 Range as a function of period for the different PBSs under consideration.

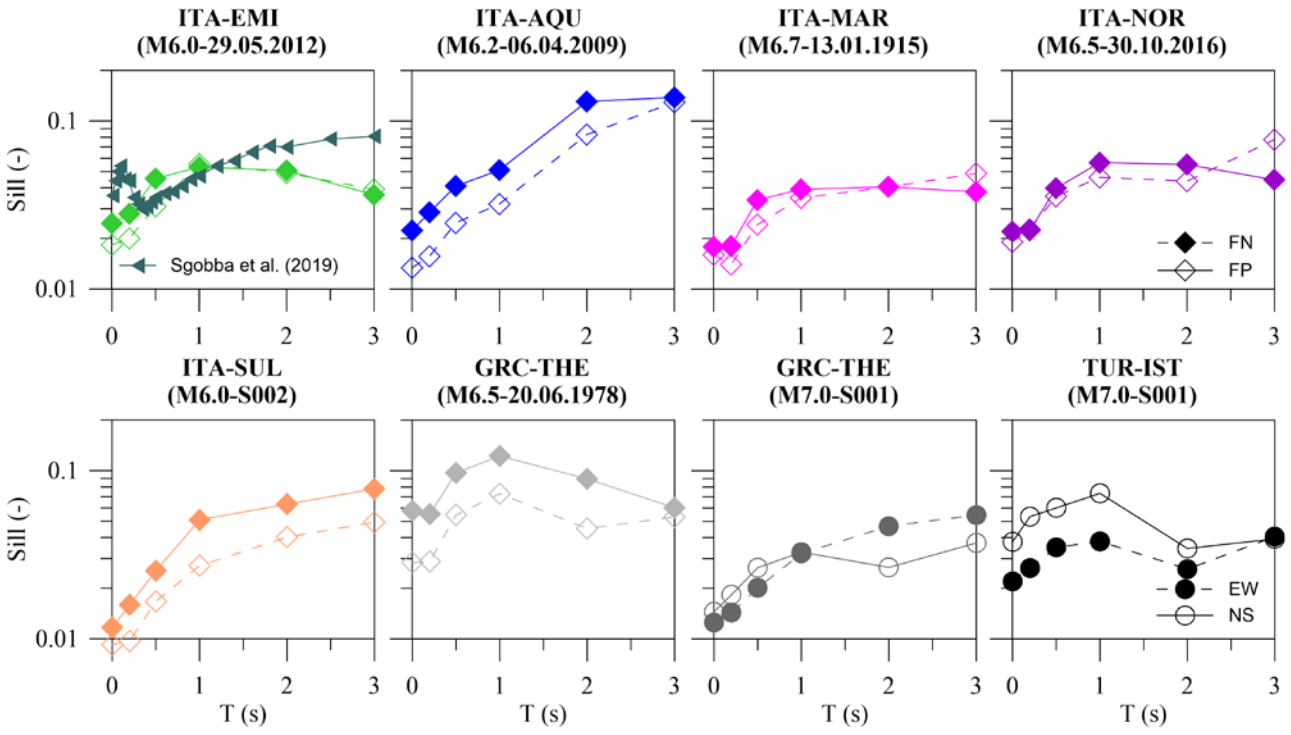

Figure 4.6 Sill as a function of period for the different PBSs under consideration.

4.3 Comparison with recordings and other studies

Comparing the spatial correlation structure of the broadband synthetics with the observed one is crucial to test the ability of the ANN2BB procedure to reproduce the actual correlation of ground motion at short periods. To this purpose, the M6 earthquake which occurred in the Po Plain (Northern Italy) on 29 May 2012

is an excellent case owing to the availability of 33 near-source recordings at epicentral distances less than 30 km. As an example, Figure 4.7 shows the semivariograms for PGA, SA(0.5s), SA(1.0s) and SA(3.0s), NS component, computed at the available accelerometric stations from both recordings (in black) and broadband simulated ground motions (BB, in red). Note that the simulated SA for $T \geq 0.75$ s are derived entirely from the 3D PBSs, while for $T < 0.75$ s they are the result of the ANN2BB procedure. The NS component is selected because it is the component where a closer match is found between PBS and recorded waveforms (see Paolucci et al. 2015). A very good agreement is found between the sample semivariograms from records and synthetics across all periods. Some differences found in the range estimates, especially at lower periods, are also related to the lower robustness of the LS regression, given the limited number of station pairs.

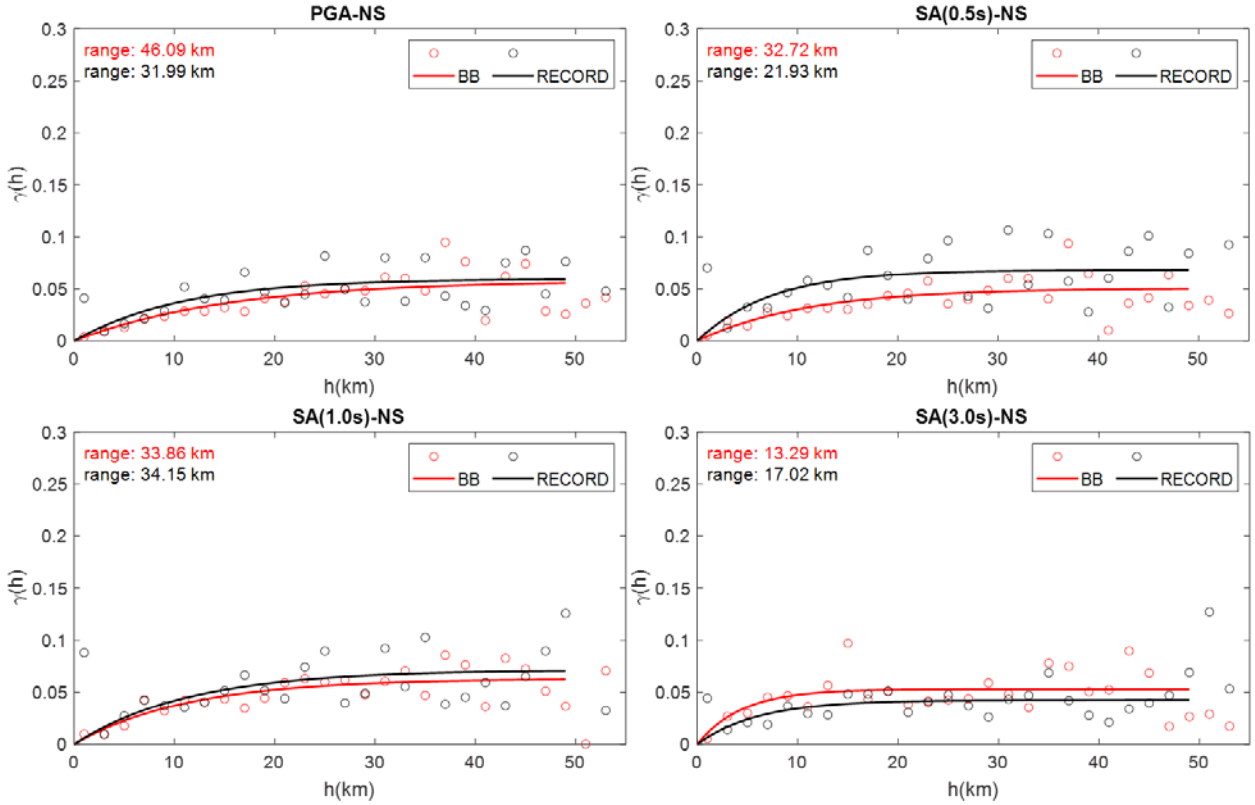

Figure 4.7 Comparison between the semivariograms computed from broadband PBS (ANN2BB, red) and recordings (black) for the 2012 Po Plain earthquake: (a) PGA, (b) SA(0.5s), (c) SA(1.0s) and (d) SA(3.0s), NS component.

As a further validation of spatial correlation estimates from PBSs, we attempted to make a rather comprehensive comparison between the ranges obtained in this study with the empirical ranges available from other published works based on earthquake recordings. Specifically, in Figure 4.8 the range (GMH component) as a function of period from PBS (for the same eight scenarios as considered previously, see Figure 4.5), is compared with the ranges computed directly on recordings (left panel, a) and with the ranges provided by empirical correlation models calibrated on the data (right panel, b). To this end, the following literature works are considered: Esposito and Iervolino (2012) based on the Italian Accelerometric Archive (ITACA) and the European Strong-Motion Database (ESD); Hong et al. (2009) on California data; Jayaram and Baker (2009) using records from the Anza, Alumn Rock, Parkfield, Chi-Chi, Northridge, Big Bear City

and Chino Hills earthquakes; Sgobba et al. (2019) on Po Plain records; Huang and Galasso (2019) on the Italian records included in the ESD.

From Figure 4.8 the following comments can be made:

- In general, the results of the present study are in reasonable agreement with those from literature, both in terms of variability of range and its trend with period;
- At different periods, range estimates are characterized by a high variability across the different regions which is consistent with the one found in literature works (see, e.g., the strong variability of range for PGA coming from Jayaram and Baker, 2009).
- Such differences may be related to different factors affecting the earthquake ground motion, ranging from the frequency content of ground motion (e.g. Baker and Jayaram, 2008; Goda and Hong, 2008), source/path effects and local geology (Sokolov et al., 2010). The dependence of the correlation structure on these factors will be discussed in detail in the following section.

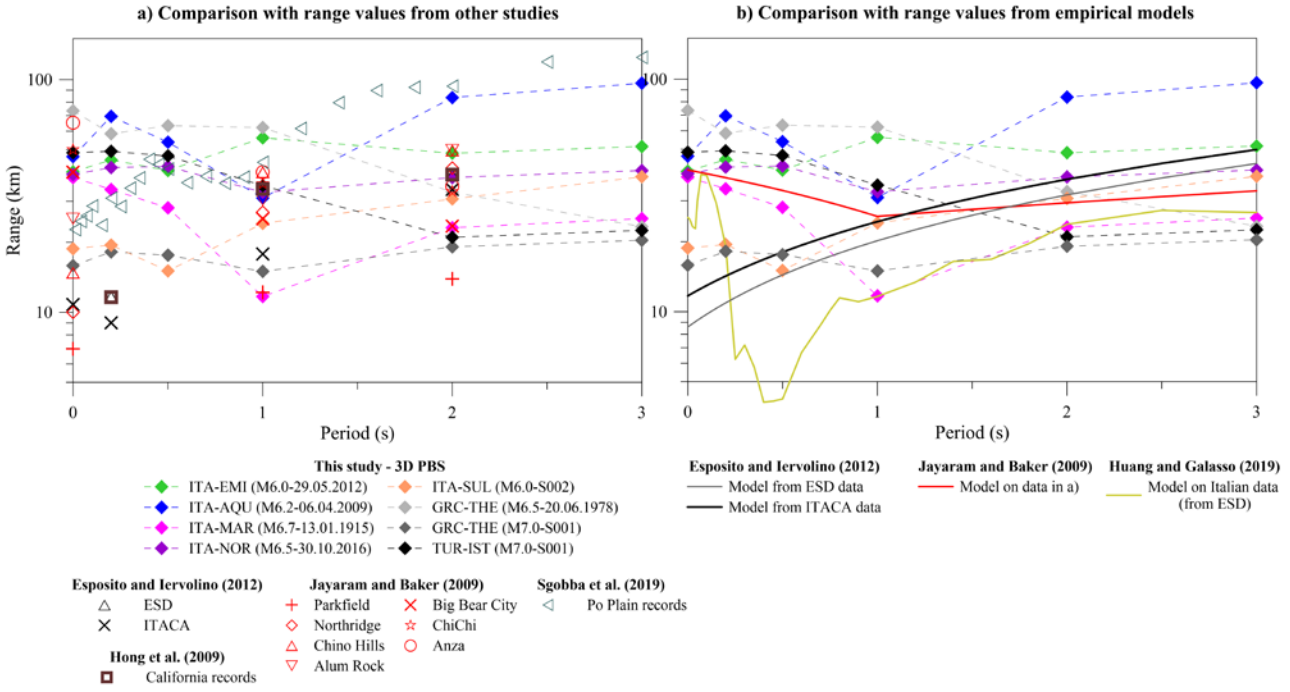

Figure 4.8 Comparison between the ranges (GMH component) estimated in this study (3D PBS) and other empirical studies. (a) Comparison with the ranges computed on recordings by Esposito and Iervolino (2012), Jayaram and Baker (2009), Hong et al. (2009) and Sgobba et al. (2019); (b) comparison with the ranges predicted by the empirical correlation models by Esposito and Iervolino (2012), Jayaram and Baker (2009) and Huang and Galasso (2019).

5. Impact of source and path effects on spatial correlation

The aim of this Section is to investigate in a systematic way the impact of various factors on spatial correlation, i.e., ground motion directionality (Section 5.1), source-related effects, such as magnitude (Section 5.2) and source directivity (Section 5.3), and path effects (Section 5.4).

5.1 Ground motion directionality: Fault Normal Vs Fault Parallel

Typically, empirical spatial correlation models are provided for the GMH component, without any distinction between the horizontal components. The dependence of the spatial correlation structure on the horizontal component of earthquake ground motion is addressed here with reference to the components parallel and normal to the causative fault (FP and FN, respectively). This aspect is relevant because the considered ground shaking scenarios are in the near-source region, where the polarization of ground motion may be significant with large FN/FP ratios (Sommerville et al., 1997).

Figure 5.1 shows the ratio of the range (left, a) and sill (right, b) for the FN over that for the FP for six representative scenarios. It is clear that the FN/FP range and sill ratios tend to be systematically larger than 1 across all periods. This means that the FN motions tend to be correlated over larger distances because, in near-fault conditions, they are more affected by source directivity effects, with longer period content and larger peak amplitudes (with distinctive pulse-like features), leading to a more coherent ground motion distribution. A similar trend is found for the sill, with higher values for FN components, consistently with the range FN/FP behavior: this means that an intrinsic higher variance is associated with FN components owing to the stronger influence of the slip asperities on the fault plane.

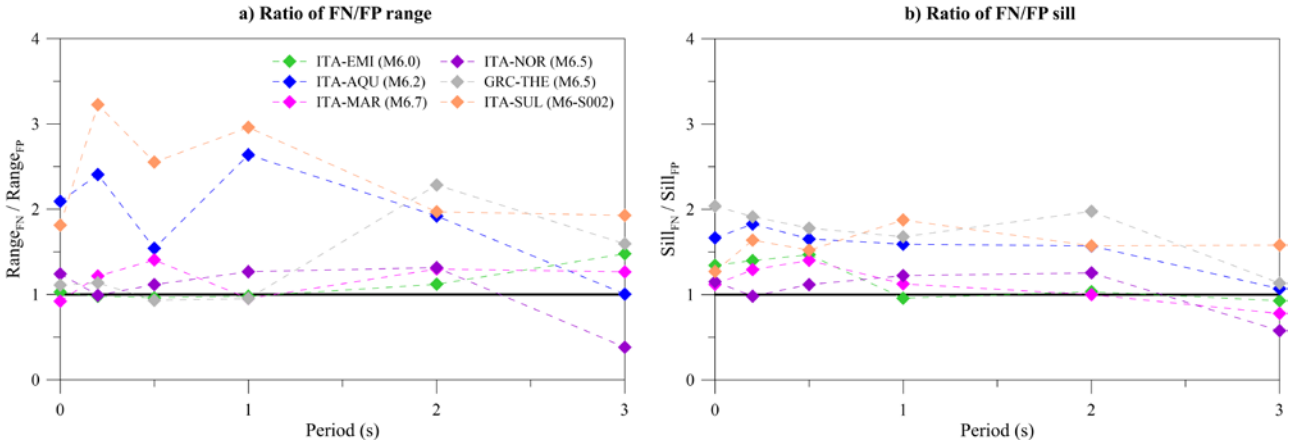

Figure 5.1 Ratio of FN/FP range (a) and sill (b) for the PBSs.

5.2 Earthquake magnitude

The availability, for the same region, of different scenarios from the same fault but with different moment magnitude (M_W) allows for the study of the possible correlation between M_W and spatial correlation (range). As an explanatory case, Figure 5.2 illustrates, for the Istanbul region, the correlation structure evaluated for two rupture scenarios along the Marmara sea segments of the North Anatolian Fault (NAF) system with M_W =7.0 (left) and M_W =7.4 (right). The semivariogram and the correlation coefficient (ρ, see Equation (4)) are provided for PGA-NS and SA(1.0s)-NS. Note that, as anticipated, a spherical model is adopted for Istanbul case. A pronounced dependence on M_W is found, with larger range and sill for increasing magnitude, owing

to the stronger energy content at low frequencies for larger events, which, in turn, yields to larger correlation. A positive correlation was also found by Sokolov et al. (2012), Sokolov and Wenzel (2013) and Foulser-Piggott and Goda (2015), consistently with this study. However, other studies (Schiappapietra and Douglas, 2020; Jayaram and Baker, 2009) did not find any clear evidence of correlation between magnitude and range, most likely because of the simultaneous presence in the recorded dataset of different factors, besides magnitude, contributing to spatial correlation.

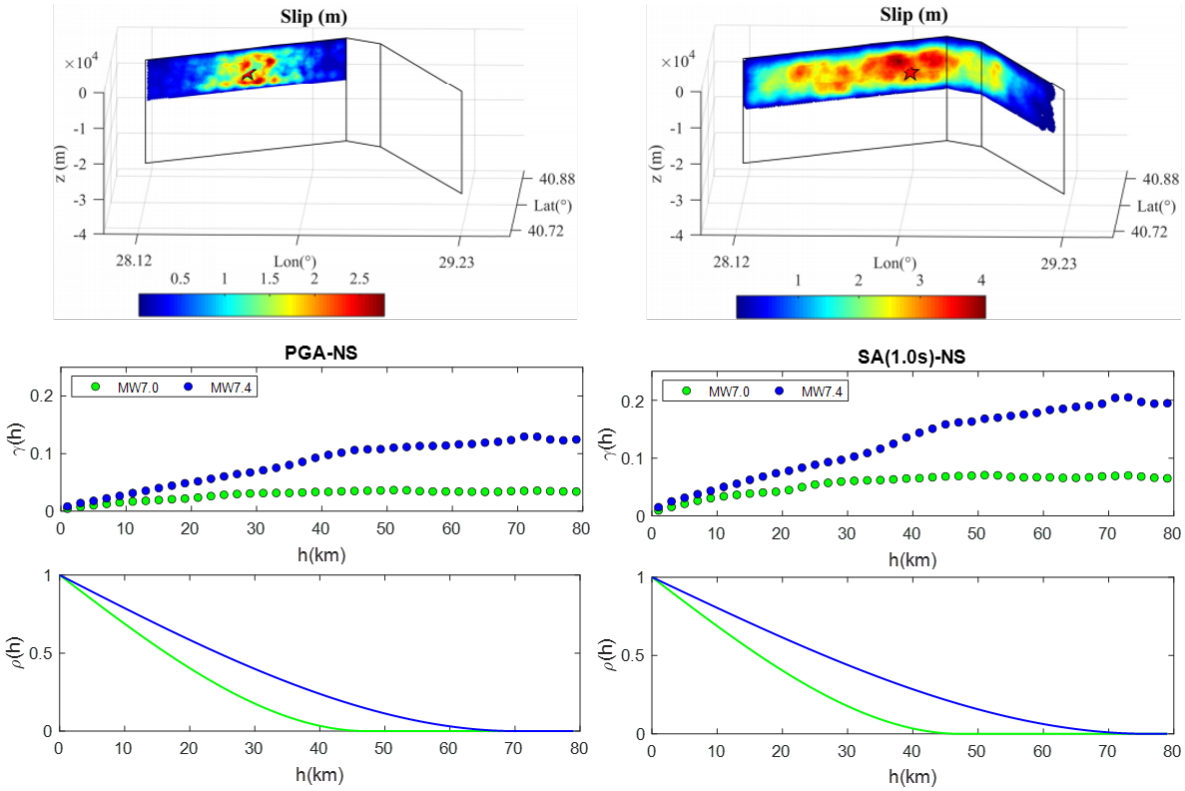

Figure 5.2 Istanbul case study. Top: fault rupture scenarios along the Marmara sea segments of the North Anatolian fault system with M_W7.0 (left) and M_W7.4 (right). Bottom: comparison of the semivariogram and correlation coefficient for the M_W7.0 (green) and M_W 7.4 (blue) scenarios for PGA-NS (left) and SA(1.0s)-NS (right).

In Figure 5.3 the range estimated for different M_W for the Sulmona (M_W = 6.0-6.5, left) and Istanbul (M_W = 7.0-7.4, right) regions are shown for both horizontal components. As previously noted, a positive correlation between M_W and range is found for both regions and for both horizontal components. This is further highlighted by Figure 5.4 depicting the range ratios of larger over lower magnitude earthquakes (M+/M-). It is noted that for increasing periods the ratio tends to decrease (especially for the Sulmona case), most likely because of the influence of other factors, such as the larger extent of the fault area with more heterogeneous slip distribution and, hence, higher variability of ground motion, which may be countertrend.

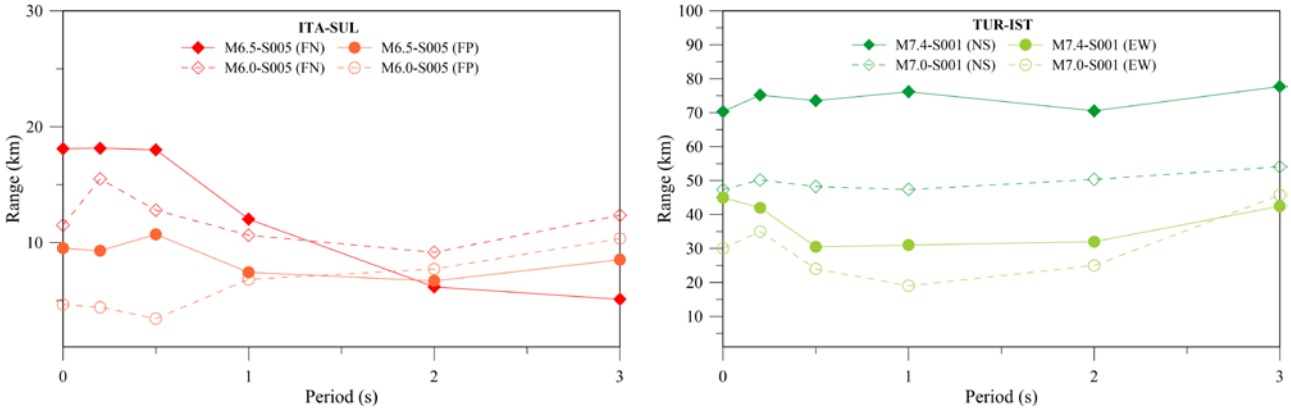

Figure 5.3 Range as a function of period for Sulmona (left), M_W6.5 Vs M_W6.0, and for Istanbul, M_W7.4 Vs M_W7.0, for both horizontal components. For each case study, filled and open symbols are for larger and lower M_W.

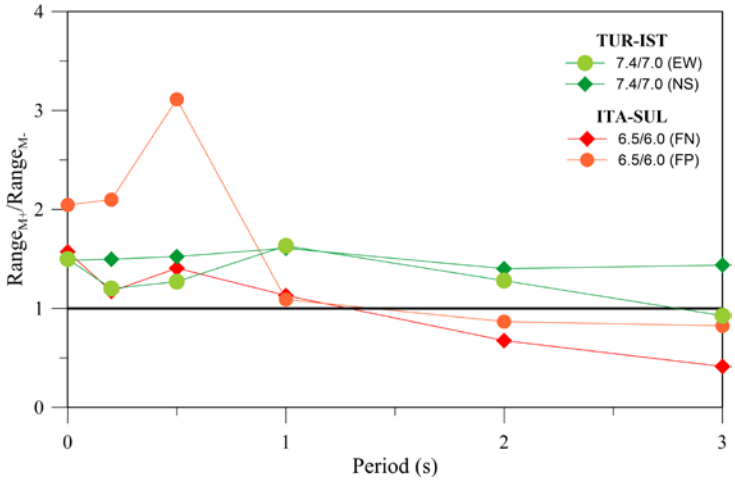

Figure 5.4 Range ratios of larger over lower magnitude earthquakes (M+/M-) for both horizontal components.

5.3 Source Directivity

We examine herein the case of three ground shaking scenarios in Istanbul area which are affected by different directivity features, namely, Forward Directivity (FD), Backward Directivity (BD) and Neutral Directivity (ND), depending on the relative position between the hypocenter and fault asperities with respect to the city of Istanbul. Note that the largest ground motion amplitudes and directivity pulses are identified especially in the NS component (which approaches the FN component given the fault strike) for the FD scenario, where the largest asperities are located along the pathway from the hypocenter to Istanbul (for a detailed discussion, see Infantino et al. 2020).

Figure 5.5 shows the map of SA(3.0s)-NS (top panel) for three selected scenarios exhibiting FD (left), BD (center) and ND (right) and the corresponding semivariograms (center panels) and correlation coefficients (bottom panels, spherical model adopted), for PGA-NS, SA(1.0s)-NS and SA(3.0s)-NS.

Results indicate that the FD scenario is characterized by higher ranges especially at long periods (larger than 1 s). To better show this effect, Figure 5.6 illustrates the range (GMH) as a function of period for the FD, BD, and ND scenarios. The reason for these effects can be understood looking at the spatial distribution of SA(3.0s): in the FD scenario, larger areas are illuminated by the rupture and are characterized by uniformly

high ground motion peak amplitudes, whereas in the BD scenario, peak values distribute less homogeneously. A clear trend cannot be found in the BD and ND scenarios, as in some cases the ND has larger ranges than BD.

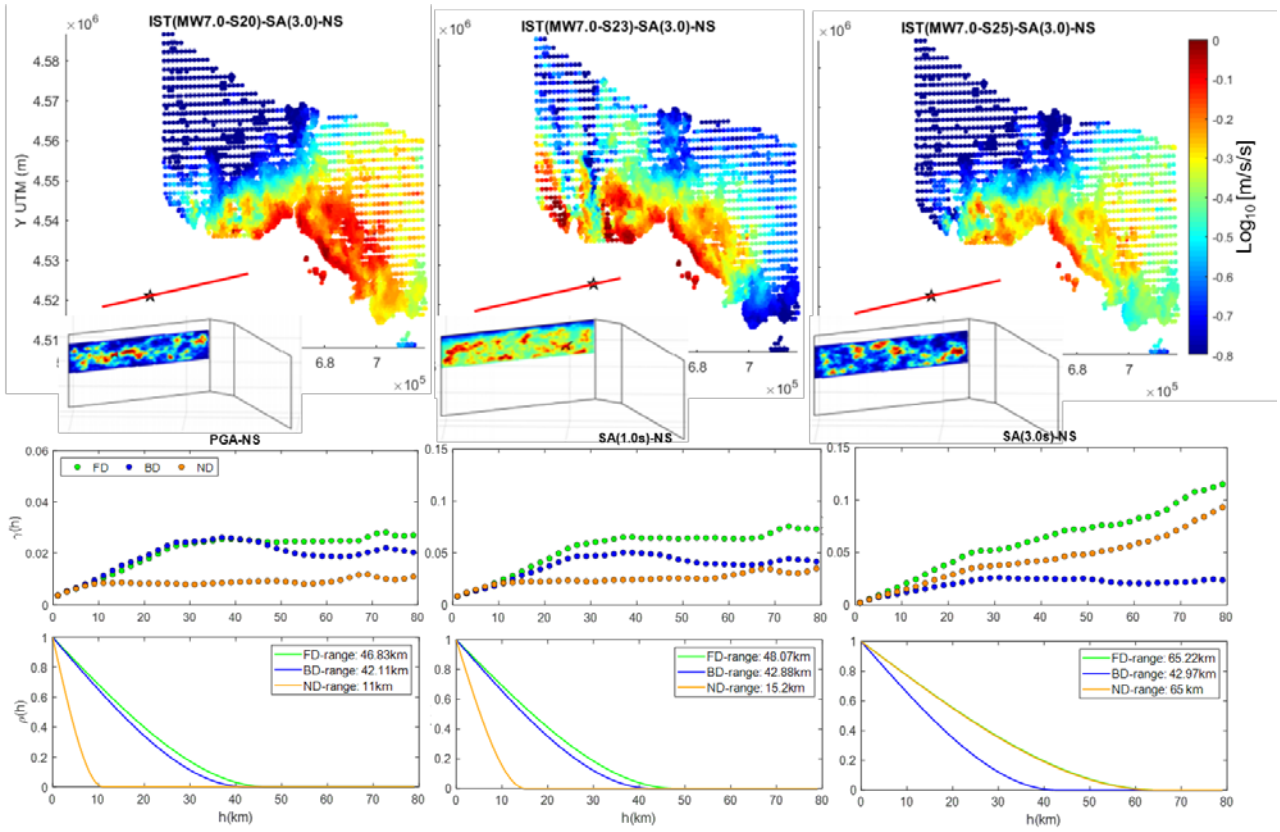

Figure 5.5 Comparison of M_W7.0 Istanbul ground shaking scenarios with Forward Directivity (FD), Neutral Directivity (ND) and Backward Directivity (BD). Top: map of SA(3s)-NS; bottom: semivariograms for PGA-NS (left), SA(1.0s)-NS (center) and SA(3.0s)-NS (right).

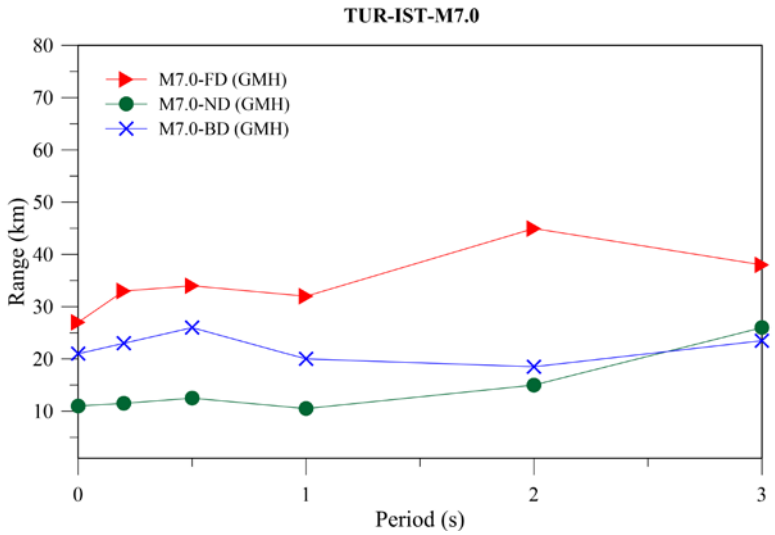

Figure 5.6 Range as a function of period for FD, BD and ND scenarios in Istanbul (see Figure 5.5), GMH component.

5.4 Path effects

The role of the propagation path from the causative fault is addressed here. To this end, the Thessaloniki model is considered (see Figure 5.7) for which two different scenarios from two faults, namely, the Gerakarou Fault (M_W=6.5, left) and the Anthemountas Fault (M_W=7.0, right) are available. The comparison of the spatial correlation coefficients, for both PGA-GMH and SA(1.0s)-GMH, indicates larger correlations for the Gerakarou scenario, even though the latter is characterized by lower magnitude. In this case, we believe that the position of the fault coupled with the soil conditions plays a predominant role. As a matter of fact, the Gerakarou fault is located at around 20 km NE of Thessaloniki on homogeneous hard rock (V_S=2000 m/s), while the Anthemountas fault is within the soft soils of the Anthemountas plain. Therefore, it is expected that coupling of fault rupture with soft soil conditions leads to more variable ground motions. This is further highlighted in Figure 5.8 where the range obtained for the Gerakarou and Anthemountas scenarios for both EW and NS components is compared.

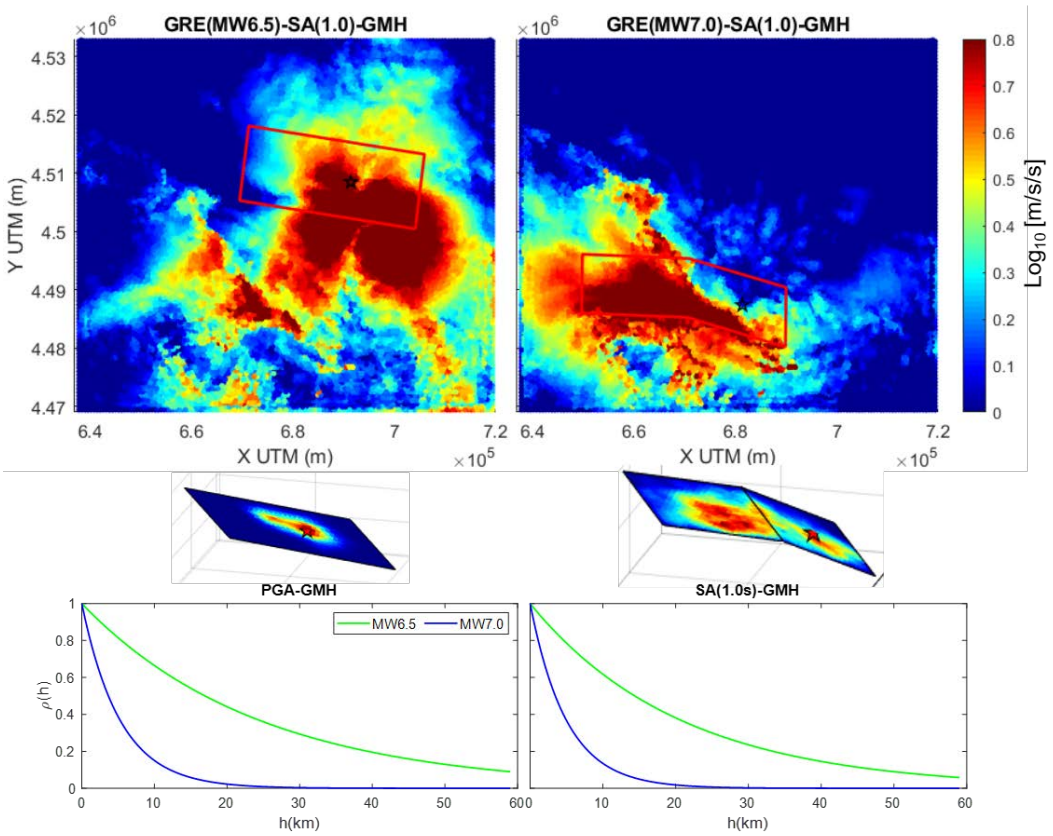

Figure 5.7 Thessaloniki ground shaking scenarios from two causative faults: Gerakarou (M_W6.5, left) and Anthemountas (M_W7.0,right). Top: map of SA(1s)-GMH; bottom: correlation coefficients for PGA-GMH (left) and SA(1.0s)-GMH (right).

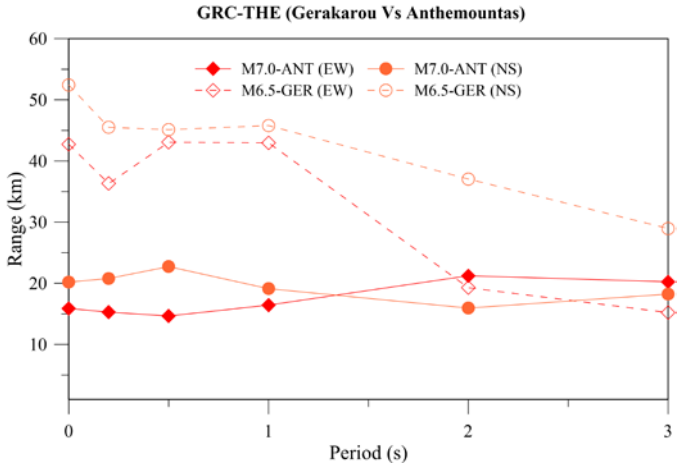

Figure 5.8 Range as a function of period for Gerakarou (GER, M_W6.5) and Anthemountas (ANT, M_W7.0) scenarios, for both EW and NS components.

6. Maps of Pearson's correlation coefficient

In this Section, the spatial correlation of PBSs ground motion residuals is estimated by means of the Pearson's correlation coefficient described in Section 3.3. Since this approach requires multiple rupture realizations of a given earthquake scenario, the Istanbul case study (Infantino et al., 2020) has been selected, for which a representative number of earthquake realizations with given M_W and fault rupture extent are available. More specifically the considered earthquake scenarios (see distribution of hypocenters in Figure 6.1) are 20 scenarios of M_W7.4 and 11 of M_W7.0. The M_W7.4 ruptures involve the entire length of the multi-segment portion of the NAF included in the numerical model (Marmara Sea segments), while the M_W7.0 ones involve only the west segment.

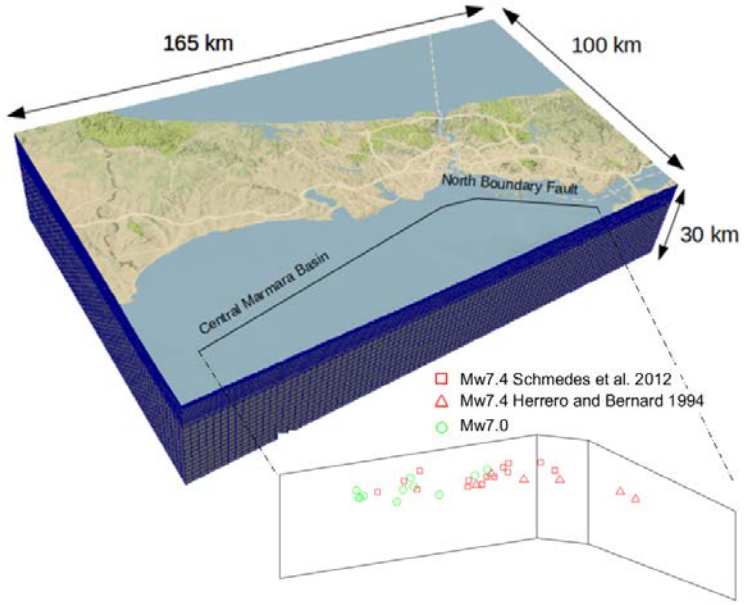

Figure 6.1 3D numerical model of Istanbul and distribution of the hypocenters of the earthquake ruptures along the Marmara Sea segments of the NAF: green circles M_W7.0 (11 ruptures), red squares M_W7.4 generated according to the HB94 source model (6 ruptures), red triangles M_W7.4 generated according to the SEA12 source model (14 ruptures).

Thus, the Pearson's correlation coefficients between each pair of sites within the urban area of Istanbul can be computed by means of Equation (11). By selecting a reference site, the correlation coefficients between the chosen reference site and all the other sites have been estimated and displayed as Pearson's correlation coefficient map (Figure 6.2, Figure 6.3 and Figure 6.4).

First of all, the effect of the geological/topographical conditions as well as of the propagation path is investigated by considering reference sites characterized by different soil properties and location with respect to the fault. Such a comparison is shown in Figure 6.2 which illustrates the Pearson's correlation maps for SA(3.0s)-GMH obtained by using the entire set of 20 M_W7.4 rupture realizations for three reference sites (from left to right, V_{S30} = 400, 1020, 1430 m/s). Moreover, below each Pearson's map the sites characterized by V_{S30} values similar to that of the reference site (within the range $\pm$ 100 m/s) are highlighted.

Comparing the three maps it is evident as the spatial pattern changes significantly as a function of the reference site. As expected, for all cases, the correlation decreases with the distance from the reference site but such a decay is not homogeneous in all the direction away from the reference site, as would expected in an isotropic case. Indeed, the propagation path, source directivity and geological conditions play a role: sites

affected by similar source directivity phenomena and characterized by similar soil and topographic properties show higher correlation.

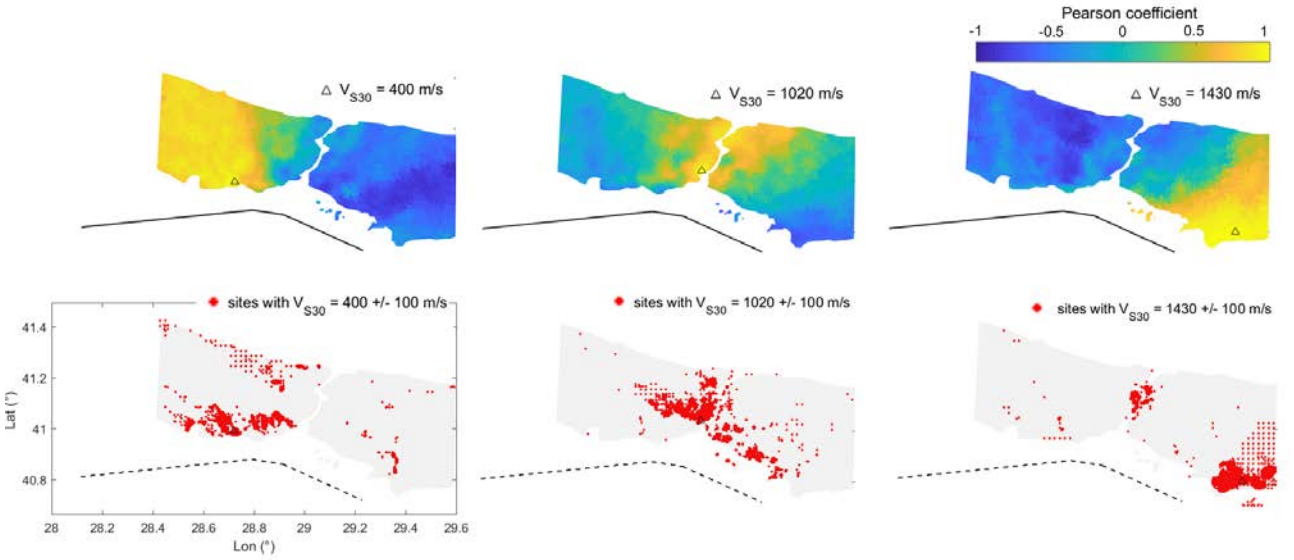

Figure 6.2 Top: Pearson's correlation coefficient maps for SA(3.0s)-GMH of 20 M_W7.4 earthquake ruptures along the NAF segments (black dashed line). The maps are shown for three reference receivers (black triangles) at different location with respect to the fault and different V_{S30} values: 400 m/s, 1020 m/s, and 1430 m/s (from the left to the right). Bottom: scattered plot of sites with values of V_{S30} similar (± 100 m/s) to that of the reference site.

As a second analysis, Figure 6.3 shows the comparison of SA(3.0s)-GMH Pearson's maps obtained using the set of M_W7.4 (left) scenarios and the set of M_W7.0 (right) for the same reference site with V_{S30}=400 m/s. The active fault for the two cases is indicated in Figure 6.3 with a solid black line (3 segment for M_W7.4 and 1 segment for M_W7.0). The different spatial correlation distributions can be explained by the source effect as a consequence of the fault extent and fault geometry/orientation. Indeed, in the case of M_W7.0, for which only the west segment breaks, strong and concentrated waveforms propagate mainly towards the west coast of the strait of Bosphorus because of the fault orientation, leading to high correlation residuals at large separation distances. On the other hand, for M_W7.4 the concave shape of the three-segmented active fault produces higher correlation of the reference site in the west region.

Finally, Figure 6.4 illustrates, for the same reference site, the correlation maps obtained with the M_W7.4 scenarios generated by two different source model, HB94 (left) and SEA12 (right). Although in both cases the reference site is positive correlated with the west region, it is found that for HB94 such correlation is almost perfect (=1) while for SEA12, although positive, it is lower than 1 and more scattered (between 0.7-0.9). Moreover, for SEA12, the correlation decays slower with distance with respect to HB94. Such differences are likely due to the slip distribution generated by the two source models (see explanatory slip distribution plots in the bottom panel of Figure 6.4). The HB94 ruptures are characterized by a more concentrated asperity along the fault leading to larger correlation over a more limited area, while SEA12 ruptures produce "scattered" asperities implying a lower maximum degree of correlation along with a slower decay with the distance.

As final remarks, it can be observed that correlation coefficients are higher in the FN direction than the FP direction while sites on opposite ends of the ruptures are negatively correlated, consistently with the findings by Chen and Baker (2019).

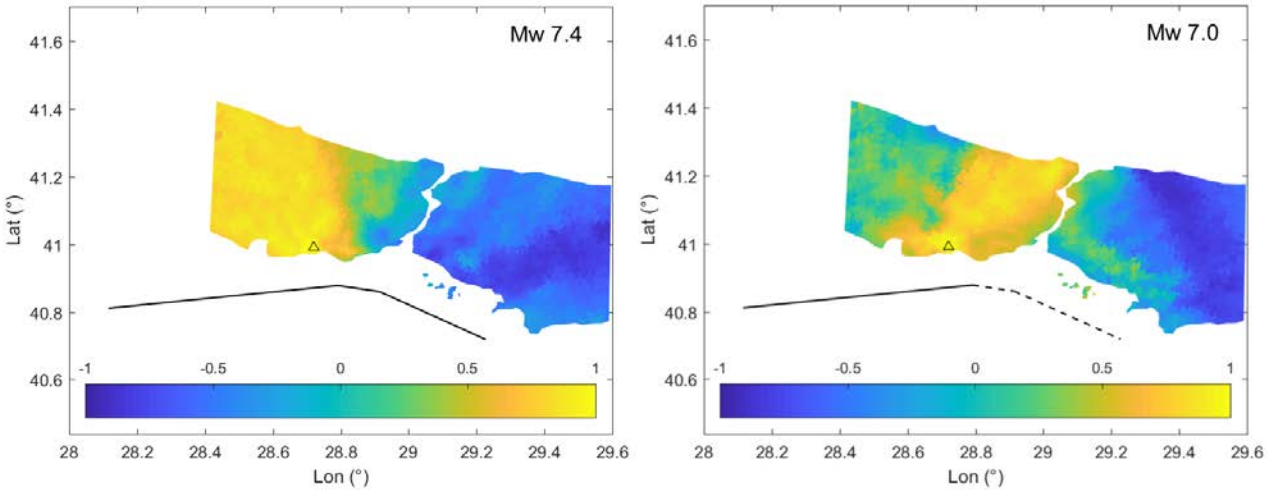

Figure 6.3 Pearson's correlation coefficient maps for SA(3.0s)-GMH of 20 M_W7.4 (left) and 11 M_W7.0 (right) for the same reference site. The causative fault considered for each case is indicated with a black solid line.

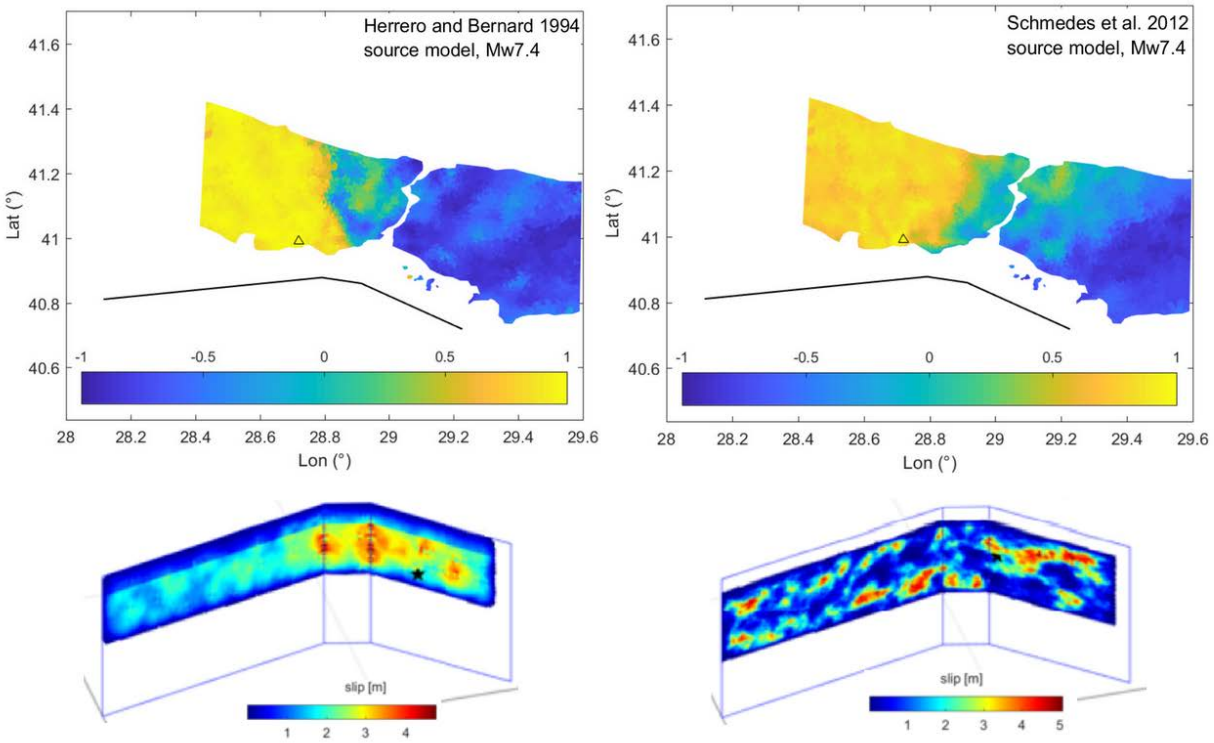

Figure 6.4 Pearson's correlation coefficient maps for SA(3.0s)-GMH of M_W7.4 ruptures scenarios according to HB94 (left) and SEA12 (right) source model.

7. Conclusions

In this work we investigated the spatial correlation in response spectral accelerations from 3D broadband physics-based numerical simulations for a wide set of rupture scenarios in seven regions worldwide, namely, Po Plain (Northern Italy), L'Aquila, Marsica, Sulmona, Norcia (Central Italy), Thessaloniki (Northern Greece), and Istanbul (Turkey). Geostatistical tools based on the calculation of both semivariograms and Pearson's correlation coefficient were applied to quantify the correlation in ground motion intra-event residuals.

Two main achievements were reached with respect to, on one hand, the validation of spatial correlation parameters from 3D PBS by comparison with both recordings and other independent studies based on strong motion datasets, and, on the other one, a systematic analysis of the impact of some relevant physical factors, such as magnitude, source directivity, propagation path and ground motion directionality, on the spatial correlation structure at different periods in near-source conditions. Such effects can be, in fact, hardly investigated using recordings due to data scarcity. The main conclusions can be summarized as follows.

Comparison with recordings and other empirical studies

- The comparison of the semivariograms computed from PBS and recordings for around 30 stations in the Po Plain area during the May 29, 2012 earthquake indicate a very good agreement at both short and long periods, thus validating the ANN2BB approach to compute broadband synthetics (Figure 4.7);
- the range estimates from PBSs for the seven regions under consideration turn out to be comparable with the empirical models available in the literature, both in terms of trend with period and overall variability (Figure 4.8);
- At different periods, range estimates are characterized by a high variability across the different regions which is consistent with the one found in literature works. This indicates that spatial variability of ground motion is region-specific, owing to its strong dependence on local geological conditions, source and path effects in near conditions.

Dependence on source, propagation path and geologic conditions

- *Ground motion directionality.* FN components turn out to be characterized by higher ranges and higher sill at both short and long periods, indicating that FN motions tend to be correlated over larger distances and have an intrinsic larger variance (Figure 5.1). This may be explained by the fact that, in near-source conditions, the FN motions are typically affected by source directivity effects which enhance longer periods (with distinctive pulse-like features), leading to a more coherent ground motion distribution. The higher variance may be associated with a stronger influence of the slip asperities on the fault plane.
- *Magnitude*. A clear positive correlation between M_W and range is found with larger ranges for increasing magnitude (Figure 5.3), owing to the stronger energy at low frequencies, consistently with other published works (e.g. Sokolov et al. 2012; Sokolov and Wenzel, 2013; Foulser-Piggott and Goda, 2015).
- *Source directivity*. For the Istanbul scenarios (strike-slip fault), for which clear forward (FD), backward (BD) and neutral directivity (ND) effects have been previously identified (Infantino et al. 2020), FD scenarios turn out to be characterized by the largest ranges especially at periods longer than 1 s and on fault-normal components (Figure 5.5). This is consistent with the observation that in FD conditions larger areas are illuminated by the rupture with more coherent "footprints" characterized by lower frequency content (Sommerville et al., 1997).

- *Propagation path and geological conditions*. For the scenarios in Thessaloniki broader area, the causative fault combined with the local geologic conditions were found to play a major role, with larger range for rupture scenarios occurring in homogeneous, rock conditions.

Anistropy and nonstationarity in spatial correlation

Although limited to the Istanbul case study and SA(3.0s)-GMH, the Pearson's correlation maps indicate that there is anisotropy and nonstationarity in spatial correlation of SA which depend on geological, source and path effects:

- Correlation is higher for sites with similar geologic conditions;
- Anisotropy: higher correlation is found for the FN direction than the FP direction;
- Nonstationarity: sites at opposite ends of the rupture tend to be negatively correlated while site along the rupture propagation path have stronger correlation.

This study identifies several factors which affect strongly spatial correlation, such as local geological conditions, source and path effects, pointing out that a single ergodic, stationarity and isotropic spatial correlation model, calibrated on a large dataset including different regions and events, may not be suitable. In this regard, 3D broadband PBS can be used as a very useful data source to either calibrate area- and scenario-specific correlation models or to provide directly the ground shaking scenarios to be used, in a Monte Carlo framework, for seismic risk assessment of urban areas, as a complementary tool to empirical ground motion models.

Further studies will address the seismic risk evaluation of infrastructural systems or spatially distributed portfolios subject to these PBS to quantify to which extent the specificity, anistropy and nonstationarity of the ground shaking scenarios may influence risk with respect to standard approaches based on GMPEs combined with a spatial correlation model for intra-event residuals.

8. References

Ancheta, T.D., Darragh, R.B., Stewart, J.P., Seyhan, E., Silva, W.J., Chiou, B.S.J., Wooddell, K.E., Graves, R.W., Kottke, A.R., Boore, D.M., Kishida, T., Donahue J.L. (2013). *PEER NGA-West2 Database, PEER Report No. 2013/03*, Pacific Earthquake Engineering Research Center, University of California, Berkeley, CA, 134 pp.

Baker, J. W. and Jayaram, N. (2008). Correlation of spectral acceleration values from NGA ground motion models. *Earthquake Spectra*, 24(1):299-317.

Cressie, N. and Hawkins, D. M. (1980). Robust estimation of the variogram: I. *Journal of the International Association for Mathematical Geology*, 12(2):115-125.

Chen, Y. and Baker, J.W. (2019). Spatial correlations in CyberShake physics-based ground-motion simulations. *Bulletin of the Seismological Society of America*, 109(6):2447-2458.

Der Kiureghian A. (1996). A coherency model for spatially varying ground motions. *Earthquake Engineering and Structural Dynamics*, 25:99-111.

Esposito, S. and Iervolino, I. (2011). PGA and PGV spatial correlation models based on European multievent datasets. *Bulletin of the Seismological Society of America*, 101(5):2532-2541.

Esposito, S. and Iervolino, I. (2012). Spatial Correlation of Spectral Acceleration in European Data. *Bulletin of the Seismological Society of America*, 102(6):2781-2788.

Evangelista, L., Del Gaudio, S., Smerzini, C., D'Onofrio, A., Festa, G., Iervolino, I., Landolfi, L., Paolucci, R., Santo, A. and Silvestri, F. (2017). Physics-based seismic input for engineering applications: a case study in the Aterno River valley, Central Italy. *Bulletin of Earthquake Engineering*, 15(7):2645-2671.

Foulser-Piggott, R. and Goda, K. (2015). Ground-motion prediction models for arias intensity and cumulative absolute velocity for Japanese earthquakes considering single-station sigma and within-event spatial correlation. *Bulletin of the Seismological Society of America*, 105(4):1903-1918.

Garakaninezhad, A. and Bastami, M. (2019). Intra-event spatial correlation model for the vertical component of response spectral accelerations. *Journal of Seismology*, 23:853-867.

Goda, K. and Hong, H. P. (2008). Spatial correlation of peak ground motions and response spectra. *Bulletin of the Seismological Society of America*, 98(1):354-365.

Goda, K. and Atkinson, G. M. (2009). Probabilistic characterization of spatially correlated response spectra for earthquakes in Japan. *Bulletin of the Seismological Society of America*, 99(5):3003-3020.

Goda, K. and Atkinson, G. M. (2010). Intra-event spatial correlation of ground-motion parameters using SK-net data. *Bulletin of the Seismological Society of America*, 100(6):3055-3067.

Herrero, A. and Bernard, P. (1994). A kinematic self-similar rupture process for earthquakes. *Bulletin of the Seismological Society of America*, 84:1216-1229.

Hong, H. P., Zhang, Y., Goda, K. (2019). Effect of spatial correlation on estimated ground-motion prediction equations. *Bulletin of the Seismological Society of America*, 99(2A):928-934.

Huang, C. and Galasso, C. (2019). Ground-motion intensity measure correlations observed in Italian strong-motion records. *Earthquake Engineering & Structural Dynamics*, 48(15):1634-1660.

Infantino, M., Mazzieri, I., Özcebe, A.G., Paolucci, R., Stupazzini, M. (2020). 3D physics-based numerical simulations of ground motion in Istanbul from earthquakes along the Marmara segment of the North Anatolian Fault. *Bulletin of the Seismological Society of America*, 110 (5): 2559-2576.

Journel, A. G., Huijbregts, C. J. (1978). Mining Geostatistics. London: Academic Press. 600 pp.

Jayaram, N. and Baker, J.W. (2009). Correlation model for spatially distributed ground motion intensities. *Earthquake Engineering and Structural Dynamics*, 38(15):1687-1708.

Jayaram, N., and J. W. Baker (2010). Considering spatial correlation in mixed-effects regression and the impact on ground-motion models, *Bulletin of the Seismological Society of America*, 100(6):3295-3303.

Matheron, G. (1965). *Les variables régionalisées et leur estimation: une application de la théorie des fonctions aléatoires aux sciences de la nature*. Paris: Masson. 305 pp.

Mazzieri, I., Stupazzini, M., Guidotti, R., and Smerzini, C. (2013). SPEED-Spectral Elements in Elastodynamics with Discontinuous Galerkin: A non-conforming approach for 3D multi-scale problems. *International Journal for Numerical Methods in Engineering*, 95:991-1010.

Ming, D., Huang, C., Peters, G. W., Galasso, C. (2019). An advanced estimation algorithm for ground-motion models with spatial correlation. *Bulletin of the Seismological Society of America*, 109(2):541-566.

Oliver, M. A. and Webster, R. (2014). A tutorial guide to geostatistics: computing and modelling variograms and kriging. *Catena*, 113:56-69.

Özcebe, A. G., Smerzini, C., Paolucci, R., Pourshayegan, H., Rodríguez Plata, R., Lai, C. G., Zuccolo, E., Bozzoni, F., Villani, M. (2019). On the comparison of 3D, 2D, and 1D numerical approaches to predict seismic site amplification: the case of Norcia basin during the M6.5 2016 October 30 earthquake. *In Proceedings of the 7th International Conference on Earthquake Geotechnical Engineering*, Rome, 17-20 June 2019.

Park, J., Bazzurro, P., Baker, J., et al. (2007). Modeling spatial correlation of ground motion intensity measures for regional seismic hazard and portfolio loss estimation. *Applications of Statistics and Probability in Civil Engineering*, 1–8.

Paolucci, R., Mazzieri, I., Smerzini, C. (2015). Anatomy of strong ground motion: near-source records and 3D physics-based numerical simulations of the Mw 6.0 2012 May 29 Po Plain earthquake, Italy, *Geophysical Journal International*, 203(3):2001-2020.

Paolucci, R., Evangelista, L., Mazzieri, I., Schiappapietra, E. (2016). The 3D numerical simulation of near-source ground motion during the Marsica earthquake, central Italy, 100 years later. *Soil Dynamics and Earthquake Engineering*, 91:39-52.

Paolucci, R., Gatti, F., Infantino, M., Smerzini, C., Özcebe, A. G., and Stupazzini, M. (2018). Broadband ground motions from 3D physics-based numerical simulations using artificial neural networks. *Bulletin of the Seismological Society of America*, 108:1272-1286.

Paolucci, R., Mazzieri, I., Piunno, G., Smerzini, C., Vanini, M., Özcebe, A.G. (2020). Earthquake ground motion modeling of induced seismicity in the Groningen gas field. Earthquake Engineering and Structural Dynamics, accepted.

Schmedes, J., Archuleta, R. J., and Lavallée, D. (2012). A kinematic rupture model generator incorporating spatial interdependency of earthquake source parameters. *Geophysical Journal International*, 192(3): 1116–1131.

Sommerville, P., Smith, N. F., Graves, R. W., Abrahamson, N. A. (1997). Modification of empirical strong ground motion attenuation relations to include the amplitude and duration effects of rupture directivity. *Seismological Research Letters*, 68(1):199-222.

Sokolov, V., Wenzel, F., Kuo-Liang, W. (2010). Uncertainty and spatial correlation of earthquake ground motion in Taiwan. *TAO: Terrestrial, Atmospheric and Oceanic Sciences*, 21(6):905-921.

Sokolov, V., Wenzel, F., Wen, K. L., Jean, W. Y. (2012). On the influence of site conditions and earthquake magnitude on ground-motion within-earthquake correlation: Analysis of PGA data from TSMIP (Taiwan) network, *Bulletin of Earthquake Engineering*, 10(5):1401-1429.

Sokolov, V. and Wenzel, F. (2013). Further analysis of the influence of site conditions and earthquake magnitude on ground-motion within-earthquake correlation: Analysis of PGA and PGV data from the K-NET and the Kik-net (Japan) networks. *Bulletin of Earthquake Engineering*, 11 (6):1909-1926.

Smerzini, C., Galasso, C., Iervolino, I., Paolucci R. (2014). Ground motion record selection based on broadband spectral compatibility, *Earthquake Spectra*, 30(4):1427-1448.

Smerzini, C., Pitilakis, K., Hashemi, K. (2017). Evaluation of earthquake ground motion and site effects in the Thessaloniki urban area by 3D finite-fault numerical simulations. *Bulletin of Earthquake Engineering*, 15(3):787–812.

Smerzini, C., Cavalieri, F., Argyroudis, S., Pitilakis, K. (2018). 3D physics-based numerical modeling as a tool for seismic risk assessment of urban infrastructural systems: the case of Thessaloniki, Greece. *16th European Conference on Earthquake Engineering*, Thessaloniki, Greece, 18-21 June 2018.

Sgobba, S., Lanzano, G., Pacor, F., Puglia, R., D'Amico, M., Felicetta, C., Luzi, L. (2019). Spatial correlation model of systematic site and path effect for ground-motion fields in northern Italy. *Bulletin of the Seismological Society of America*, 109(4):1419-1434.

Schiappapietra, E. and Douglas, J. (2020). Modelling the spatial correlation of earthquake ground motion: Insights from the literature, data from the 2016_2017 Central Italy earthquake sequence and ground-motion simulations. *Earth-Science Reviews*, 203:103-109.

Villani, M., Faccioli, E., Ordaz, M. and Stupazzini, M. (2014). High-Resolution seismic hazard analysis in a complex geological configuration: the case of the Sulmona basin in central Italy. *Earthquake Spectra*, 3(4):1801-1824.

Wang, M. and Takada, T. (2005). Macrospatial correlation model of seismic ground motions. *Earthquake Spectra,* 21(4):1137-1156.

Weatherill, G., Silva, V., Crowley, H., and Bazzurro, P. (2015). Exploring the impact of spatial correlations and uncertainties for portfolio analysis in probabilistic seismic loss estimation. *Bulletin of Earthquake Engineering*, 13(4):957-981.

Zerva, A. and Zerva, V. (2002). Spatial variation of seismic ground motions: An overview. *Applied Mechanics Reviews*, 55(3): 271-297.

Zimmerman, D. L. and Stein, M. (2010). Classical geostatistical methods. *Handbook of Spatial Statistics*. Boca Raton, FL：CRC Press .

Appendix A

For each case study, the following graphs are provided

- Summary sheet on the numerical model and main simulation parameters: velocity model, mesh properties, references, on-line repository;
- Summary sheet on the case study for computation of spatial correlation: receiver map, fault rupture scenario, site proxies (i.e. H_{bed} and V_{Seq}[2]);
- Spatial correlation calculations for PGA and SA(1.0s), for both FN and FP components: map of IM (log_{10}); map of residuals (log_{10}); sample semivariogram $\gamma(h)$ and best-fitting exponential model.

[2] $V_{S,eq}$ – time averaged shear-wave velocity from the surface to H_{800} (if $H_{800} \leq 30$ m; if $H_{800} > 30$ m, then H_{800}=30m),

ITA_EMI		
COUNTRY	**LOCATION**	**FAULT**
ITA	PO PLAIN	MIRANDOLA

VELOCITY MODEL

(1) BASIN / SUPERFICAL MODEL

Geological unit	Depth z (m)[(i)]	ρ (kg/m³)[(ii)]	V_S (m/s)[(ii)]	V_p (m/s)[(ii)]	Q_s(-) [(iii)]	Damping Type[(iv)]	Soil [(v)]
Quaternary	<150	1800	300	1500	30	FP	NLVE
	[150,z_Q]	c_1=1800, c_2=6, c_3=150	c_1=300, c_2=10, c_3=150	c_1=1500, c_2=10, c_3=150	$Q_0=V_s(z)/10$ F_0=0.67	FP	NLVE
Pliocene	(z_Q,z_P]	c_1=2100, c_2=4, c_3=z_Q	c_1=800, c_2=15, c_3=z_Q	c_1=2000, c_2=15, c_3=z_Q	$Q_0=V_s(z)/10$ F_0=0.67	FP	NLVE

[(i)] z_Q and z_P denotes the base of the Quaternary and Pliocene

[(ii)] ρ, V_S, $V_p = c_1 + c_2 \cdot (z-c^3)^{0.5}$

[(iii)] $Q_S = (Q_o \cdot f)/f_o$, f is the frequency in Hz

[(iv)] FP: frequency proportional

[(v)] NLVE: Non linear visco-elastic

(2) CRUSTAL MODEL

Geological Unit	Depth z(m)	ρ (kg/m³)	V_S (m/s)	V_p (m/s)	Q_s (-)	Damping Type
Before Pliocene	(z_P,500]	2100	800	1800	80	FP
	(500,1000]	2100	1200	2300	150	FP
	(1000,3000]	2200	2100	3500	200	FP
	(3000,6000]	2400	2750	4750	250	FP
	>6000	2800	3670	6340	350	FP

MESH

Model Volume ($km \times km \times km$)	#Elements	Spectral Degree	Δt (s)	Duration (s)	Fmax (Hz)
$74 \times 51 \times 20$	1'975'240	3	10^{-3}	30	1.5

REFERENCES

Publications & Reports	Paolucci et al. (2015). Anatomy of strong ground motion: near-source records and three-dimensional physics-based numerical simulations of the Mw 6.0 2012 May 29 Po Plain earthquake, Italy, *Geophysical Journal International* **203** , 2001-2020
Link to Website / Repository	http://speed.mox.polimi.it/WebRepository/

ITA_2012.05.29_09.00lt_Mw6.0	
Map of Receivers	Fault Rupture Scenario
	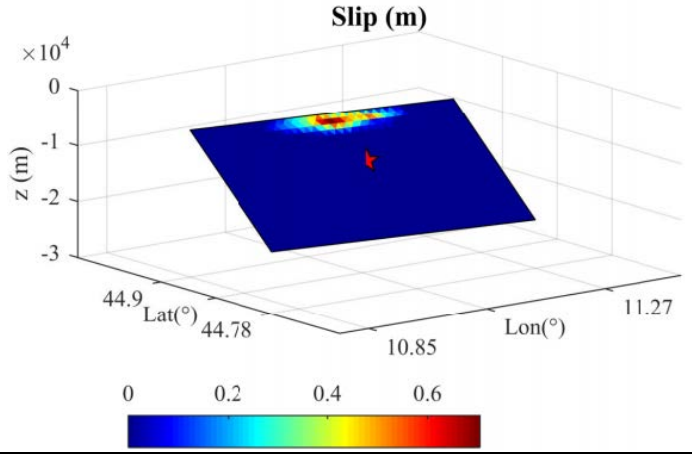
Site Proxy: Depth to bedrock (H_{bed})	Site Proxy: Equivalent Shear Wave Velocity ($V_{S,eq}$)
	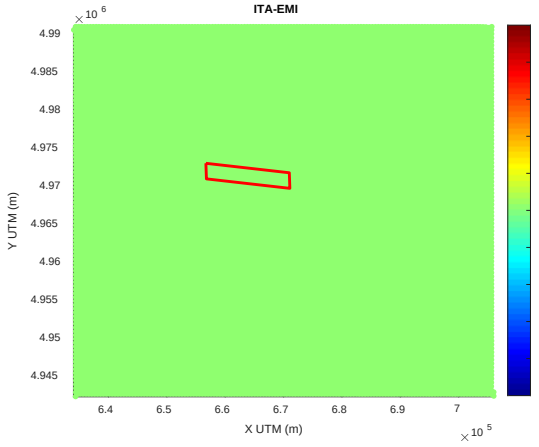

ITA_2012.05.29_09.00lt_Mw6.0

	FN Component	FP Component
PGA	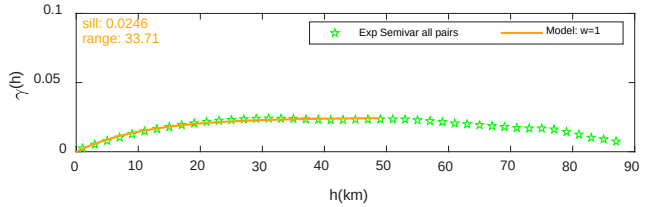	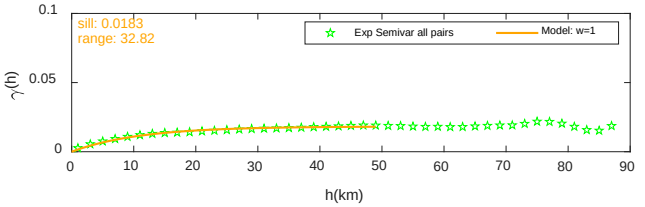
SA(1s)	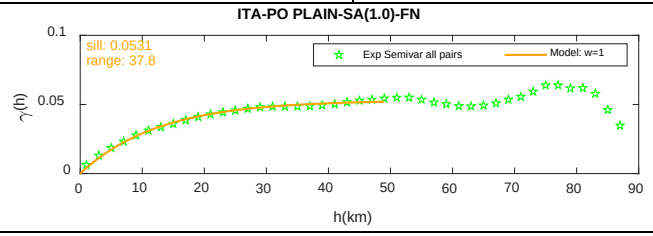	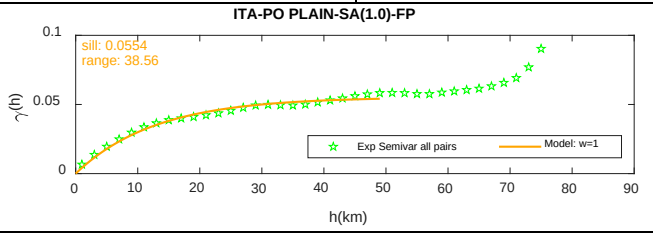

ITA_AQU		
COUNTRY	**LOCATION**	**FAULT**
ITA	L'AQUILA	PAGANICA

VELOCITY MODEL

(1) BASIN / SUPERFICAL MODEL

Geological unit	Depth z (m)[(i)]	ρ (kg/m³)	V_S (m/s)[(ii)]	V_p (m/s)[(iii)]	Q_s(-) [(iv)]	Damping Type[(v)]	Soil [(vi)]
Holocene-Pleistocene	$z<z_{HP}$	1900	c_1=300, c_2=36, c_3=0.43	R_{PS} = $4.57^{0.5}$	Q_o = $V_s(z)/10$ F_o=0.67	FP	LVE

[(i)] z_{HP} denotes the base of the Holocene and Pleistocene deposits

[(ii)] $V_S = c_1 + c_2 \cdot z^{c3}$

[(iii)] $V_p = R_{pS} \cdot V_S$

[(iv)] $Q_S = (Q_o \cdot f)/f_o$, f is the frequency in Hz

[(v)] FP: frequency proportional

[(vi)] LVE: linear visco-elastic

(2)CRUSTAL MODEL

Depth z (m)	ρ (kg/m³)	V_S (m/s)	V_p (m/s)	Q_s (-)	Q_p (-)	Damping Type
(z_{HP},1000]	2500	1700	3160	100	300	FP
(1000,2000]	2840	2600	4830	200	450	FP
(2000,5000]	2940	3100	5760	200	550	FP
(5000,20000]	3180	3500	6510	200	650	FP

MESH

Model Volume ($\mathrm{km}\times\mathrm{km}\times\mathrm{km}$)	#Elements	Spectral Degree	Δt (s)	Duration (s)	Fmax (Hz)
$58\times58\times20$	3×10^5	3	10^{-3}	30	≈ 2

REFERENCES

Publications & Reports	Evangelista et al. (2017). Physics-based input for engineering applications: a case study in the Aterno river valley, Central Italy, *Bull earthquake Eng* **15,** 2645-2671
Link to Website / Repository	http://speed.mox.polimi.it/WebRepository/

<table>
<tr><th colspan="2">ITA_2009.04.06_03.32lt_Mw6.2</th></tr>
<tr><td>Map of Receivers</td><td>Fault Rupture Scenario</td></tr>
<tr><td></td><td> 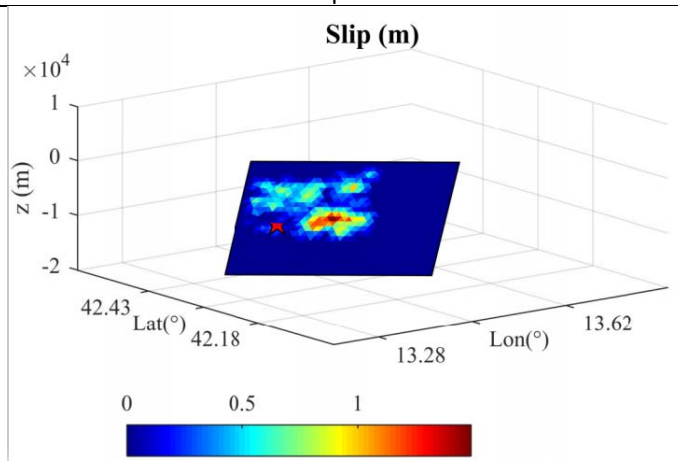
</td></tr>
<tr><td>Site Proxy: Depth to bedrock (H_{bed})</td><td>Site Proxy: Equivalent Shear Wave Velocity ($V_{S,eq}$)</td></tr>
<tr><td> 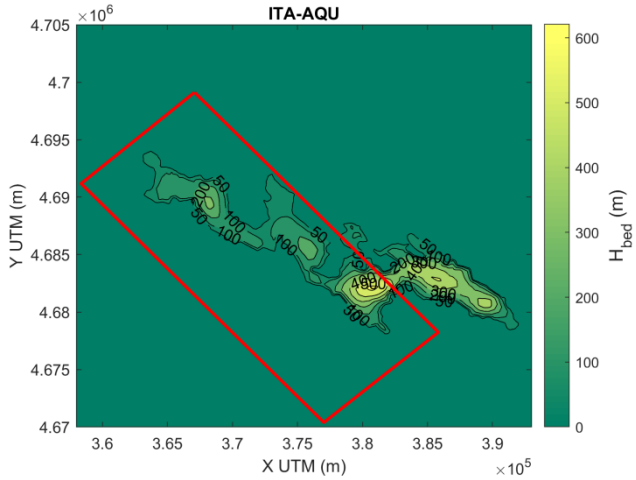
</td><td> 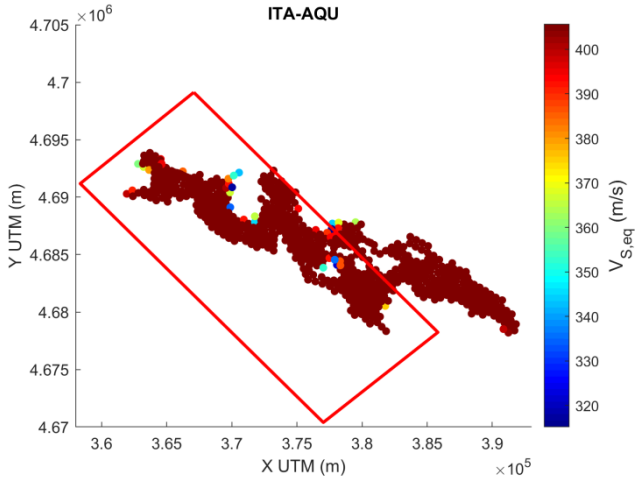
</td></tr>
</table>

ITA_2009.04.06_03.32lt_Mw6.2

	FN Component	FP Component
PGA	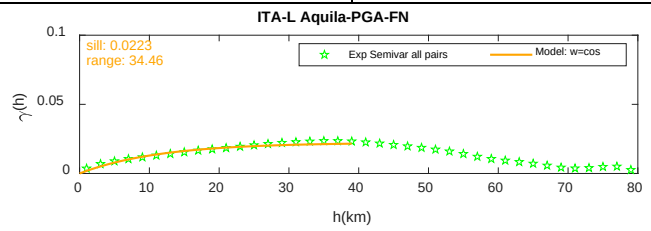	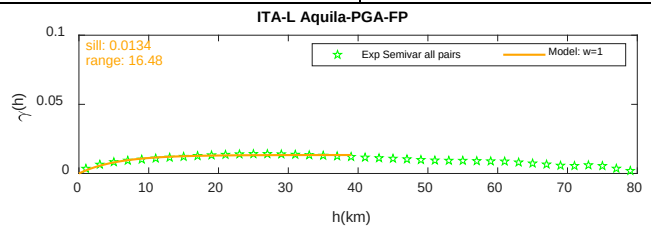
SA(1s)	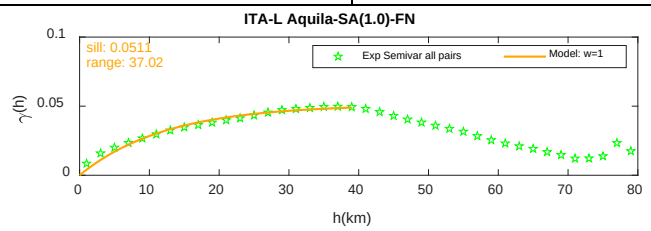	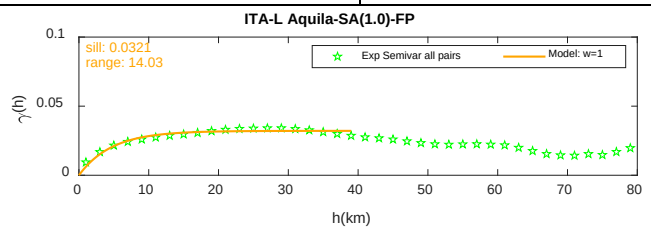

ITA_MAR		
COUNTRY ITA	**LOCATION** MARSICA	**FAULT** FUCINO

VELOCITY MODEL

(1) BASIN / SUPERFICAL MODEL

Geologic unit	**Depth z (m)**[(i)]	**ρ (kg/m³)**[(ii)]	**V_S (m/s)**[(ii)]	**V_p (m/s)**[(iii)]	**Q_s(-)** [(iv)]	**Damping Type**[(v)]	**Soil** [(vi)]
Pleistocene/ Quaternary	$[0,z_B]$	c_1=1530, c_2=10, c_3=0.54	c_1=180, c_2=10, c_3=0.60	$R_{PS} = 10^{0.5}$	$Q_0 = V_s(z)/10$ F_0=0.5	FP	NLVE

[(i)] z_B : depth of the Fucino basin

[(ii)] ρ, $V_S = c_1 + c_2 \cdot z^{c3}$

[(iii)] $V_p = R_{pS} \cdot V_S$

[(iv)] $Q_S = (Q_o \cdot f) / f_o$, f is the frequency in Hz

[(v)] FP: frequency proportional

[(vi)] NLVE: Non linear visco-elastic

(2)CRUSTAL MODEL

Geological Unit	**Depth z(m)**	**ρ (kg/m³)**	**V_S (m/s)**	**V_p (m/s)**	**Q_s (-)**	**Damping Type**
Meso-Cenozoic carbonate	$(z_B,500]$	2300	1000	1800	100	FP
	(500,1000]	2500	1700	3160	150	FP
	(1000,2000]	2840	2600	4830	250	FP
	(2000,5000]	2940	3100	5760	300	FP
	(5000,20000]	3180	3500	6510	350	FP

MESH

Model Volume ($km \times km \times km$)	**#Elements**	**Spectral Degree**	**Δt (s)**	**Duration (s)**	**Fmax (Hz)**
$56 \times 46 \times 20$	464.470	4	0.2	50	2.0

REFERENCES

Publications & Reports	Paolucci et al. (2016). The 3D numerical simulation of near source ground motion during the Marsica earthquake, central Italy, 100 years later, *Soil Dynamics and Earthquake Engineering* **91**, 39-52
Link to Website / Repository	http://speed.mox.polimi.it/WebRepository/

<table>
<tr><th colspan="2">ITA_1915.01.13_06.52lt_Mw6.7</th></tr>
<tr><td>Map of Receivers</td><td>Fault Rupture Scenario</td></tr>
<tr><td></td><td> 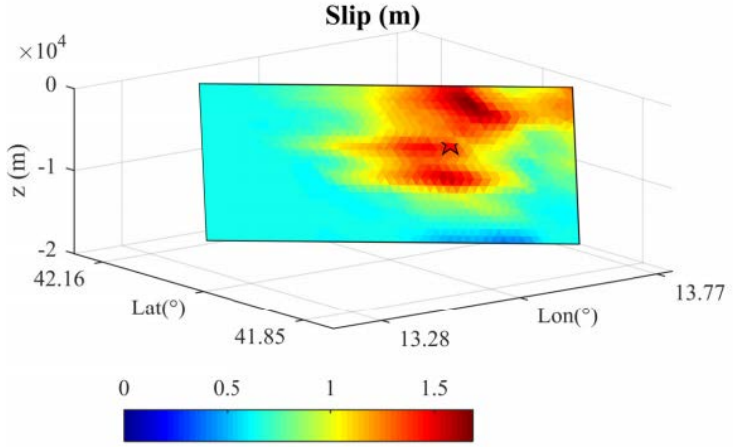
</td></tr>
<tr><td>Site Proxy: Depth to bedrock (H_{bed})</td><td>Site Proxy: Equivalent Shear Wave Velocity ($V_{S,eq}$)</td></tr>
<tr><td></td><td> 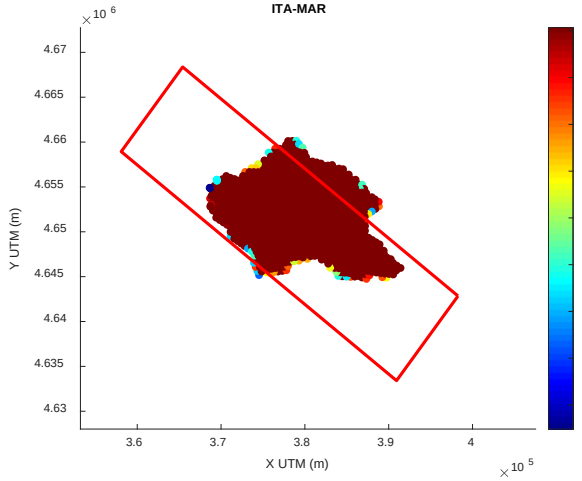
</td></tr>
</table>

ITA_1915.01.13_06.52lt_Mw6.7

	FN Component	FP Component
PGA	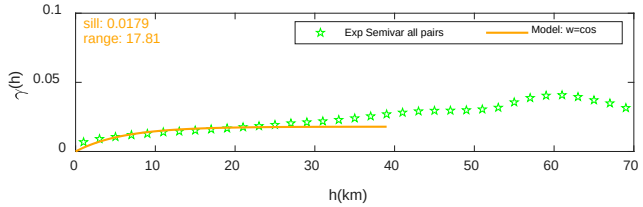	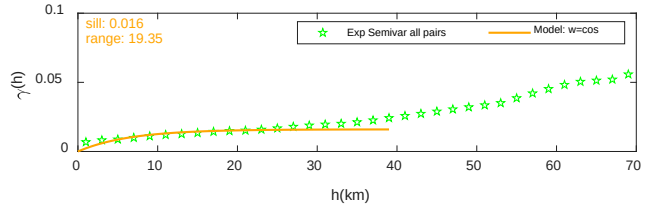
SA(1s)	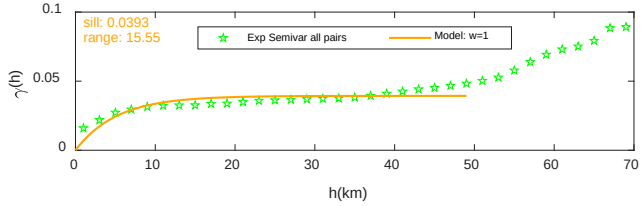	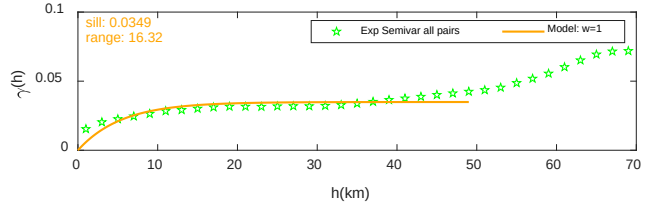

ITA_NOR		
COUNTRY	**LOCATION**	**FAULT**
ITA	NORCIA	Mt.VETTORE

VELOCITY MODEL

(1) BASIN / SUPERFICAL MODEL

Geological unit[(i)]	**Depth z (m)**[(ii)]	**ρ (kg/m³)**[(iii)]	**V_S (m/s)**[(iv)]	**V_p (m/s)**[(v)]	**Q_s(-)** [(vi)]	**Damping Type**[(vii)]	**Soil** [(viii)]
AN2/AN3	(0,150]	c_1=1900, c_2=0.35	$V_{s,min}$=281.64 V_s(z=15m)=584.33 n=1.29	R_{PS} = 1.855	Q_0 = V_s(z)/10 F_0=0.50	FP	NLVE
	[150,z_{AN}]	c_1=1900, c_2=0.35	975	R_{PS} = 1.855	Q_0 = V_s(z)/10 F_0=0.50	FP	NLVE

[(i)] AN2: alluvial fan conglomerates of Pleistocene age; AN3: heterometric conglomerates of Lower-Pleistocene age

[(ii)] z_{AN} : depth of the AN conglomerates, <400 m

[(iii)] $\rho = c_1 + c_2 \cdot z$

[(iv)] $$Vs(z) = Vs,\min + \frac{2\times[Vs(z=15m) - Vs,\min]}{1+(15/z)^n}$$

[(v)] $V_p(z)=R_{PS} \cdot V_S(z)$

[(vi)] $Q_S = (Q_o \cdot f)/f_o$, f is the frequency in Hz

[(vii)] FP: frequency proportional

[(viii)] NLVE: Non linear visco-elastic

(2)CRUSTAL MODEL

Geological Unit	**Depth z(m)**	**ρ (kg/m³)**	**V_S (m/s)**	**V_p (m/s)**	**Q_s (-)**	**Q_P (-)**	**Damping Type**[(i)]
Neogene and Quaternary	(z_{AN},1000]	2500	1700	3160	200	400	FP
	(1000,2000]	2840	2600	4830	200	400	FP
	(2000,5000]	2940	3100	5760	200	400	FP
	(5000,21000]	3150	3500	6510	200	400	FP

MESH

Model Volume ($km \times km \times km$)	**#Elements**	**Spectral Degree**	**Δt (s)**	**Duration (s)**	**Fmax (Hz)**
$40 \times 50 \times 21$	350000	3	0.0002	40.0	1.5

REFERENCES

Publications & Reports	Comparison of different approaches for the evaluation of seismic site amplification effects: the case study of Norcia (contributors: POLIMI-UniPV)
Link to Website / Repository	http://speed.mox.polimi.it/WebRepository/

<table>
<tr><th colspan="2">ITA_2016.10.30_07.40lt_Mw6.5</th></tr>
<tr><td>Map of Receivers</td><td>Fault Rupture Scenario</td></tr>
<tr><td></td><td> 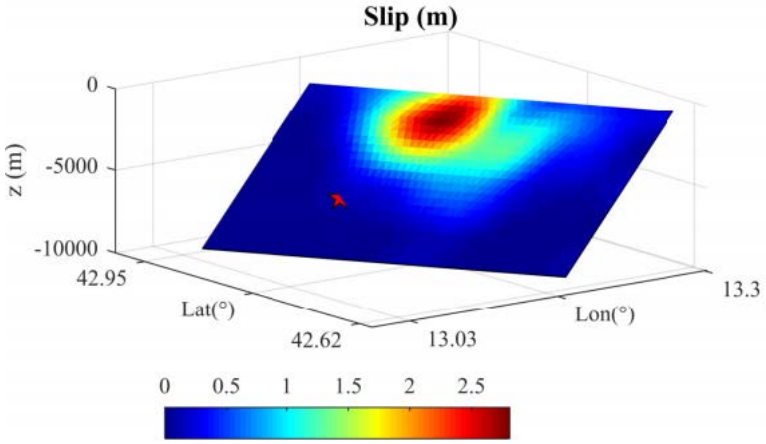
</td></tr>
<tr><td>Site Proxy: Depth to bedrock (H_{bed})</td><td>Site Proxy: Equivalent Shear Wave Velocity ($V_{S,eq}$)</td></tr>
<tr><td> 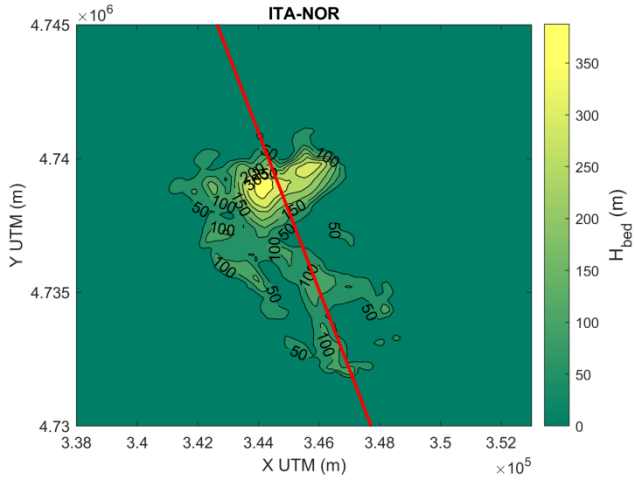
</td><td> 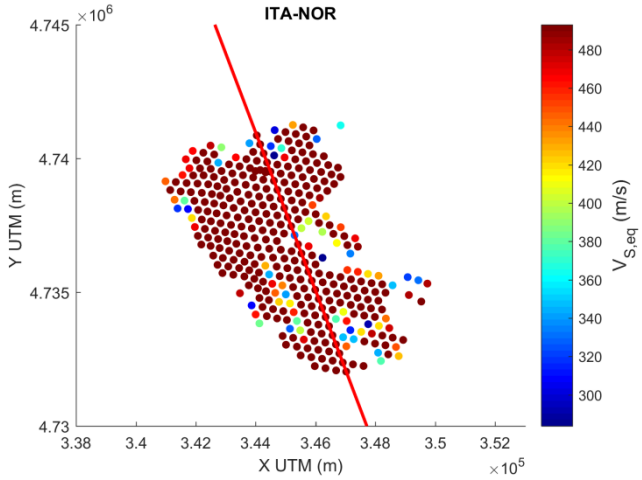
</td></tr>
</table>

ITA_2016.10.30_07.40lt_Mw6.5

	FN Component	FP Component
PGA	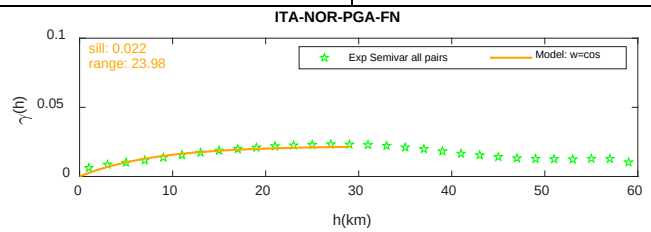	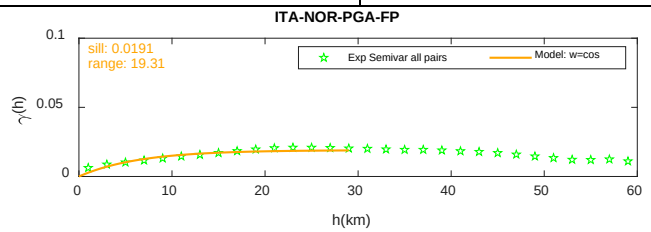
SA(1s)	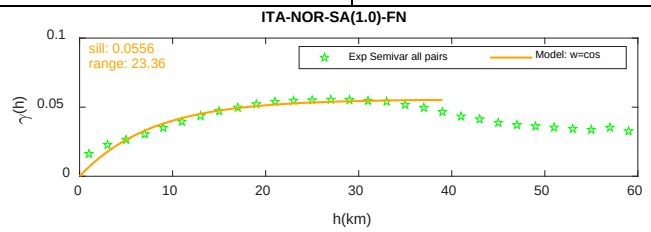	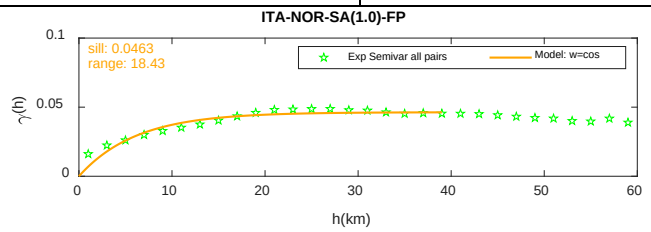

ITA_SUL		
COUNTRY ITA	**LOCATION** SULMONA	**FAULT** MT. MORRONE

VELOCITY MODEL

(1) BASIN / SUPERFICAL MODEL

Geologic unit	Depth z (m)[(i)]	ρ (kg/m³)[(ii)]	V_S (m/s)[(ii)]	V_p (m/s)[(ii)]	Q_s(-)	Q_p(-)	Damping Type[(iii)]	Soil [(iv)]
Quaternary	$[0,z_B]$	c_1=1900, c_2=0.125, c_3=1	c_1=500, c_2=19, c_3=0.50	c_1=1000, c_2=1.2, c_3=1	$V_S(z)/10$	$V_S(z)/10$	FP	LVE

[(i)] z_B : depth of the Sulmona basin

[(ii)] ρ, V_S, $V_p = c_1 + c_2 \cdot z^{c_3}$

[(iii)] FP: frequency proportional

[(iv)] LVE: Linear visco-elastic

(2)CRUSTAL MODEL

Geological Unit	Depth z(m)	ρ (kg/m³)	V_S (m/s)	V_p (m/s)	Q_s (-)	Damping Type
Quaternary	$(z_B,900]$	2000	1200	2400	75	FP
	(900,3750]	2400	2200	4000	100	FP
	(3750,4750]	2600	2666	4800	150	FP
	(4750,7750]	2800	3055	5500	250	FP
	(7750,13950]	2900	3500	6300	300	FP

MESH

Model Volume ($km \times km \times km$)	#Elements	Spectral Degree	Δt (s)	Duration (s)	Fmax (Hz)
$49.4 \times 41.7 \times 13.2$	370,857	3	10^{-3}	30	2.5

REFERENCES

Publications & Reports	Villani et al. (2014). High-Resolution seismic hazard analysis in a complex geological configuration: the case of the Sulmona basin in central Italy, *Earthquake Spectra* **3(4)**, 1801-1824
Link to Website / Repository	http://speed.mox.polimi.it/WebRepository/

ITA_SUL_MMF_MW6.0_S001/S002/S003/S004/S005

Map of Receivers	Proxy: Equivalent Shear Wave Velocity ($V_{S,eq}$)	Site Proxy: Depth to bedrock (H_{bed})
	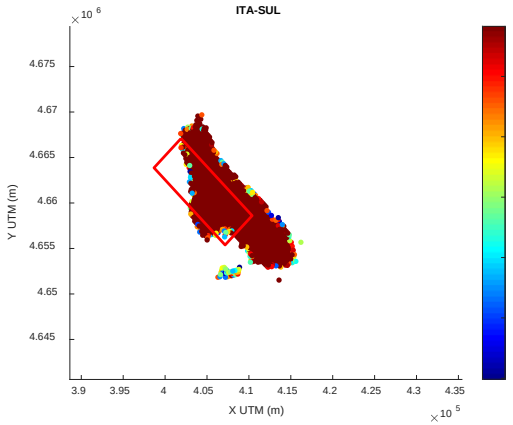	

Slip distributions

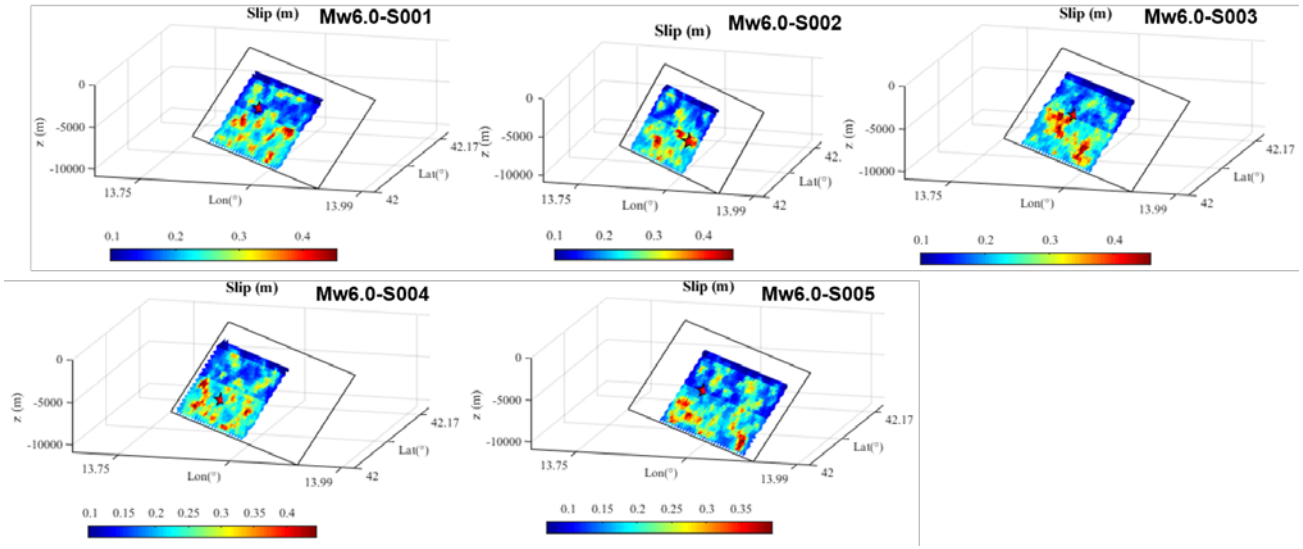

ITA_SUL_MMF_MW6.0_S001

	FN Component	FP Component
PGA	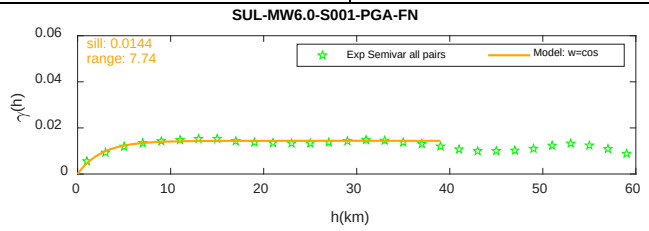	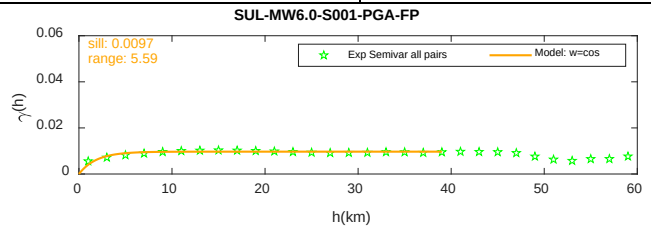
SA(1s)	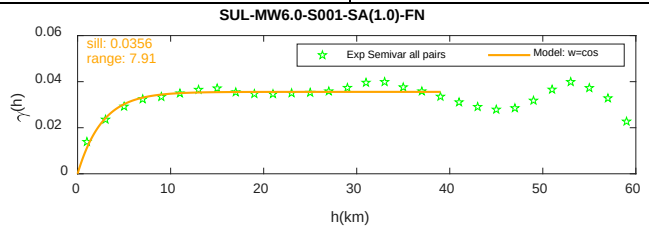	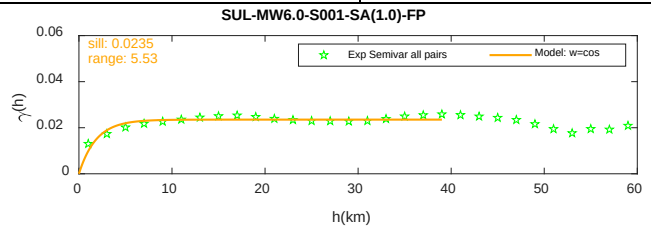

ITA_SUL_MMF_MW6.0_S002

	FN Component	FP Component
PGA	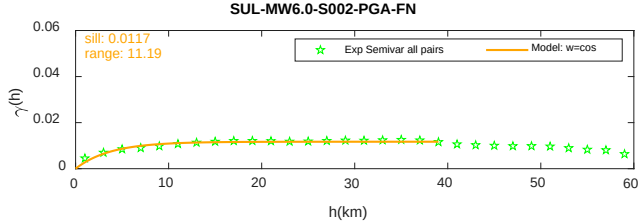	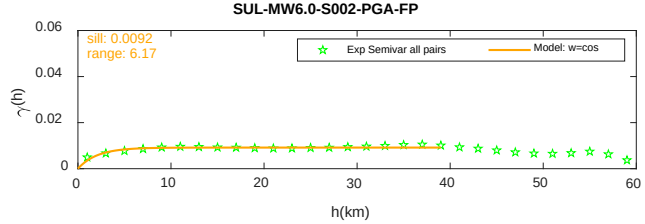
SA(1s)	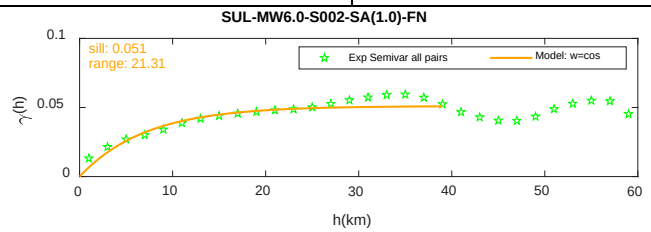	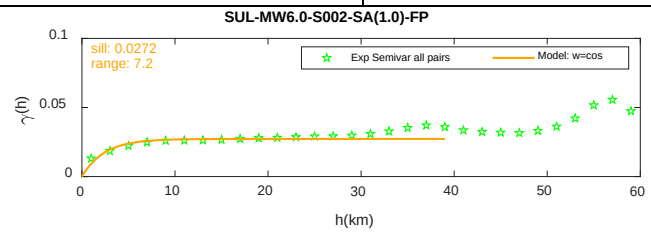

ITA_SUL_MMF_MW6.0_S003

	FN Component	FP Component
PGA	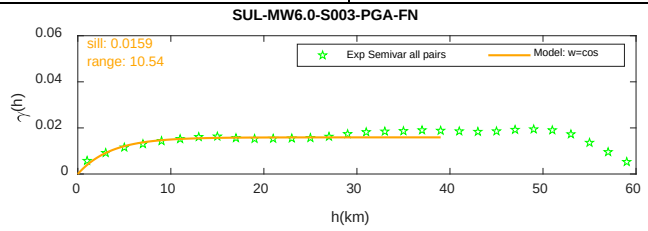	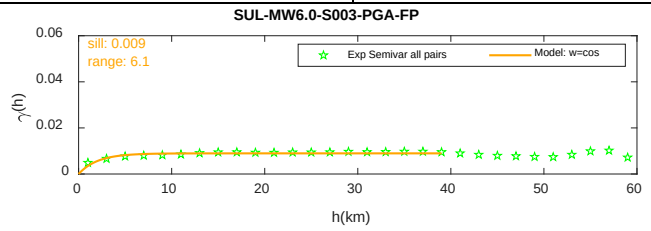
SA(1s)	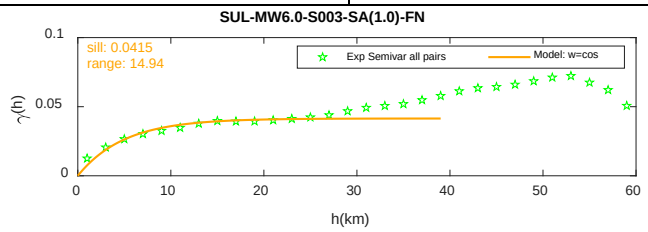	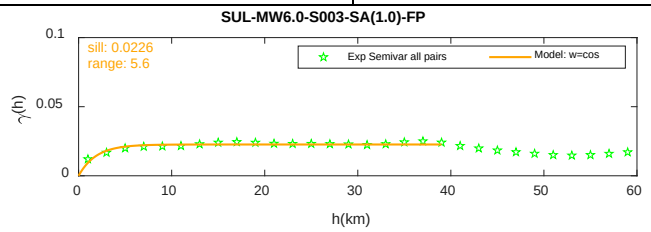

ITA_SUL_MMF_MW6.0_S004

	FN Component	FP Component
PGA	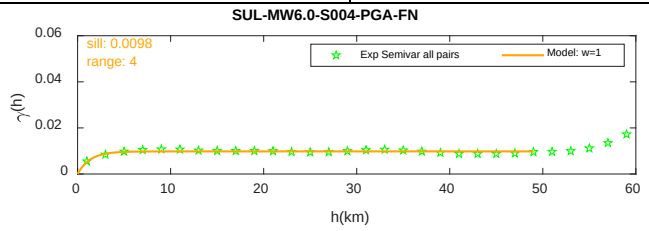	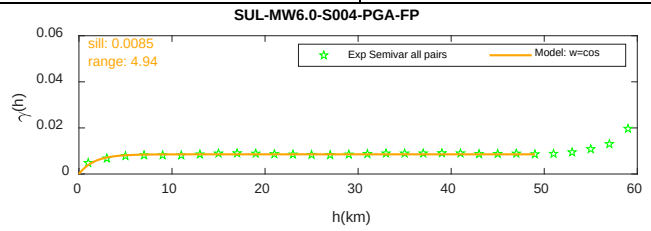
SA(1s)	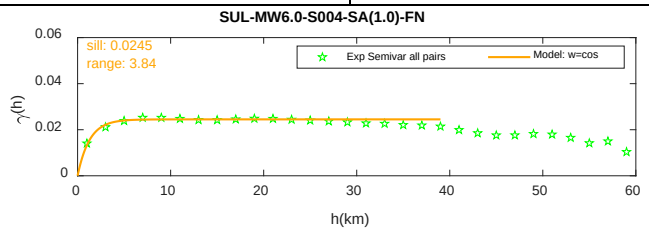	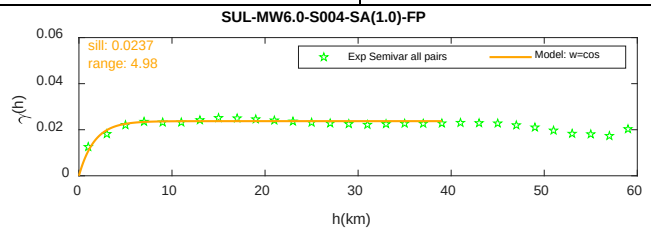

ITA_SUL_MMF_MW6.0_S005

	FN Component	FP Component
PGA	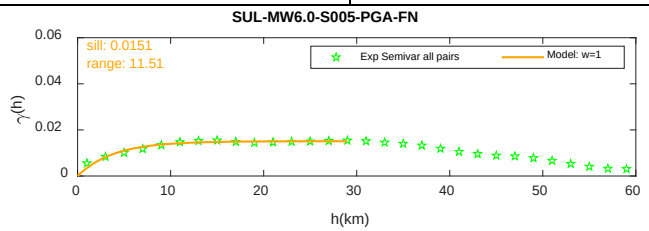	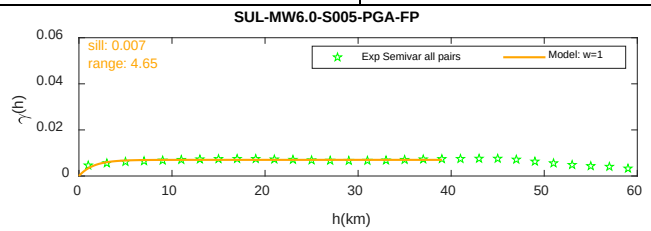
SA(1s)	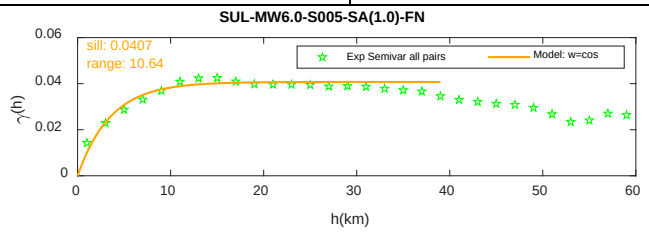	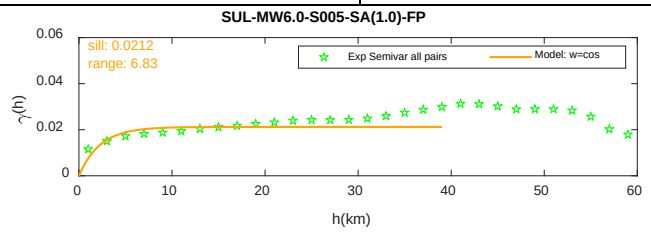

ITA_SUL_MMF_MW6.5_S002/S003/S005

Map of Receivers	Proxy: Equivalent Shear Wave Velocity ($V_{S,eq}$)	Site Proxy: Depth to bedrock (H_{bed})
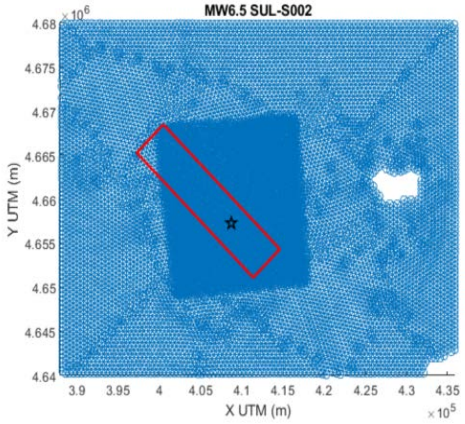	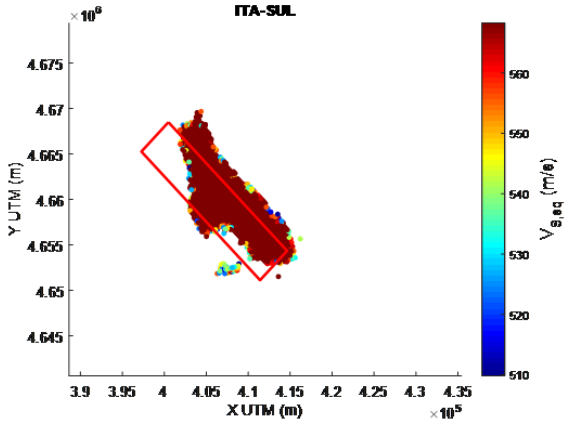	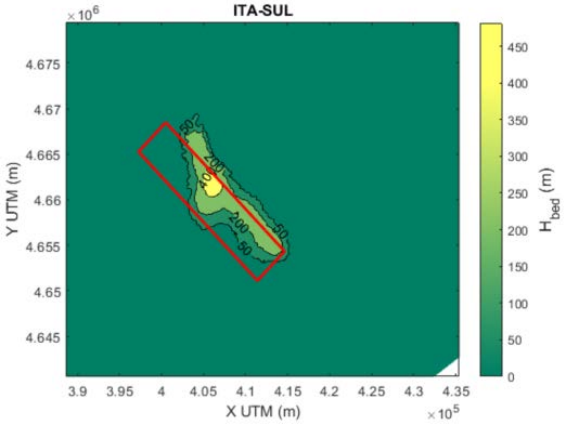

Slip distributions

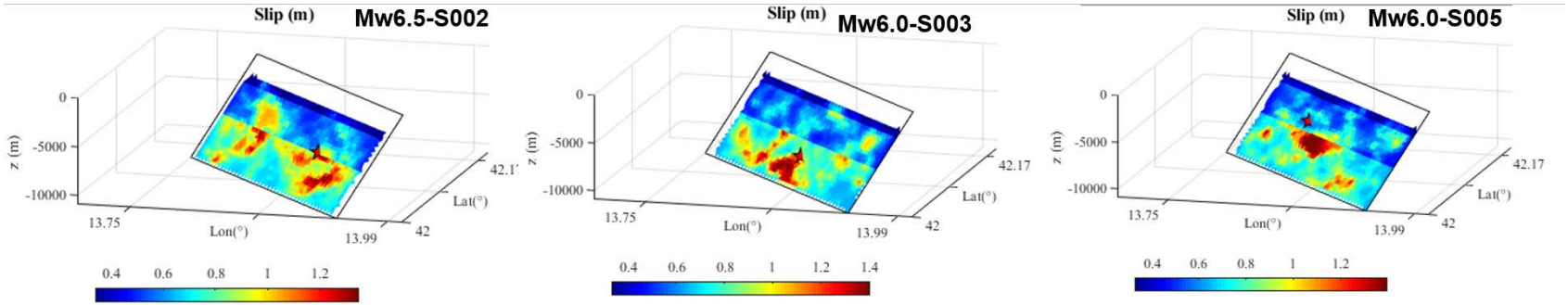

ITA_SUL_MMF_MW6.5_S002

	FN Component	FP Component
PGA	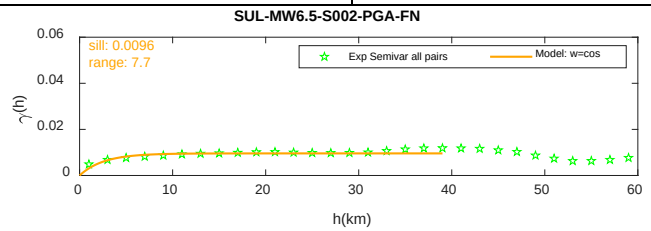	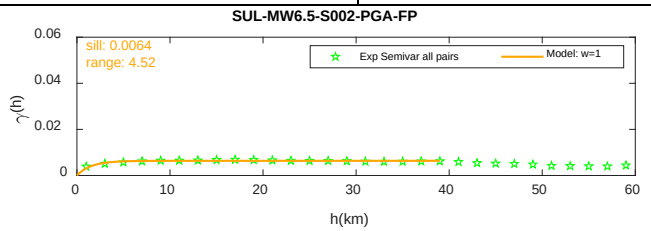
SA(1s)	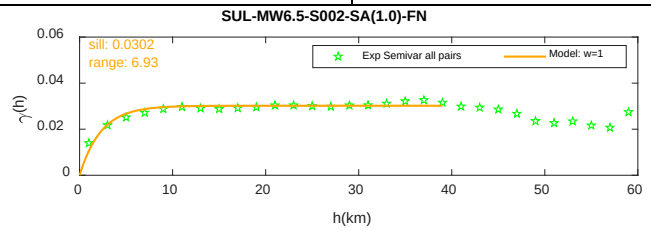	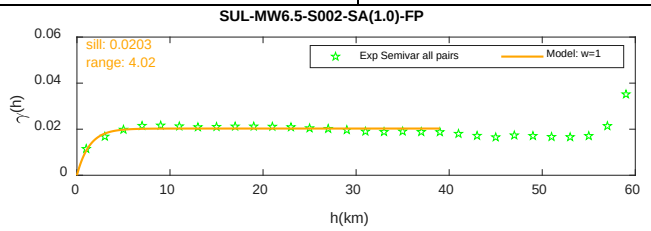

ITA_SUL_MMF_MW6.5_S003

	FN Component	FP Component
PGA	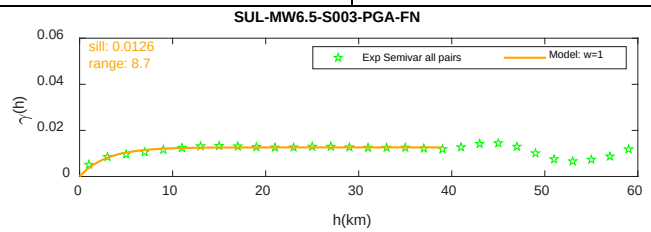	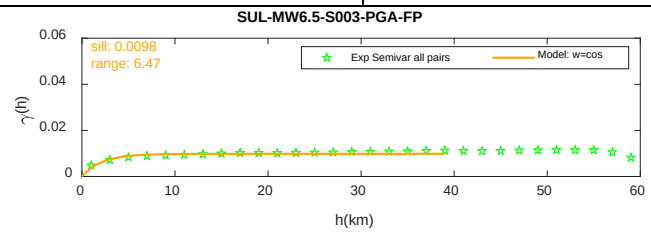
SA(1s)	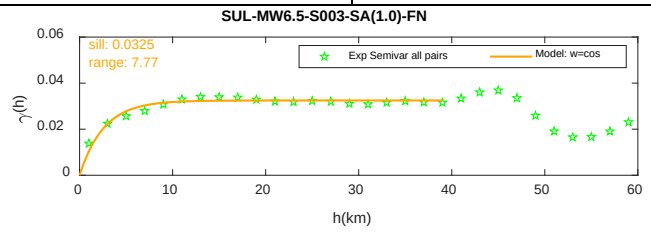	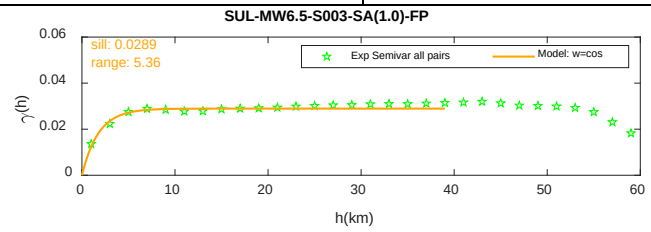

ITA_SUL_MMF_MW6.5_S005

	FN Component	FP Component
PGA	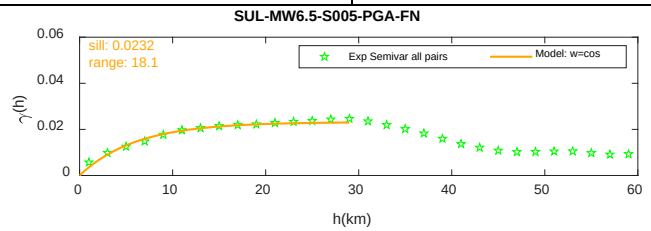	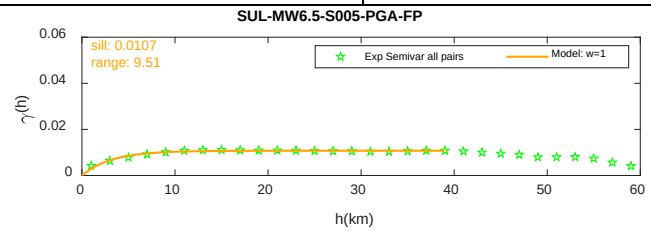
SA(1s)	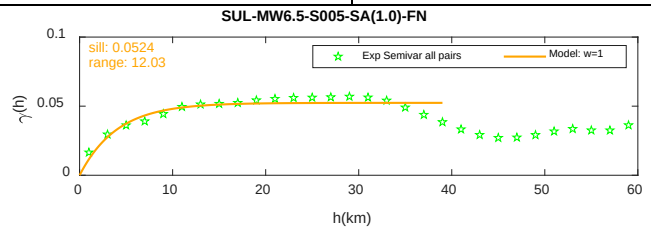	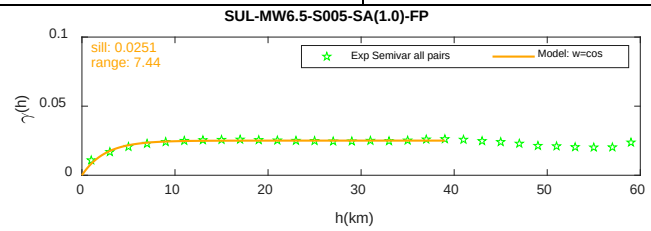

GRC_THE		
COUNTRY	**LOCATION**	**FAULT**
GRC	THESSALONIKI	GERAKAROU

VELOCITY MODEL

(1) BASIN / SUPERFICAL MODEL

Geological unit	**Depth z (m)**[(i)]	**ρ (kg/m³)**[(ii)]	**V_S (m/s)**[(ii)]	**V_p (m/s)**[(ii)]	**Q_s(-)** [(iii)]	**Damping Type**[(iv)]	**Soil** [(v)]
Holocene	$(0,z_B]$	c_1=2000, c_2=2400, c_3=1	c_1=500/300, c_2=2000, c_3=0.60	c_1=2000/1800, c_2=4500, c_3=0.70	$Q_o = V_s(z)/10$ F_o=0.67	FP	NLVE

[(i)] z_B : The depth of basin

[(ii)] ρ, V_S ,$V_p = c_1 + (c_2 - c_1) \cdot (z/h)^{c3}$, h=1000m (the maximum depth of profile up to geologic bedrock)

[(iii)] $Q_S = (Q_o \cdot f)/f_o$, f is the frequency in Hz

[(iv)] FP: frequency proportional

[(v)] NLVE: Non Linear visco-elastic

(2)CRUSTAL MODEL

Geological Unit	**Depth z(m)**	**ρ (kg/m³)**	**V_S (m/s)**	**V_p (m/s)**	**Q_s (-)**	**Damping Type**
Neogene and Quaternary	$(z_B$,1000]	2400	2000	4500	200	FP
	(1000,5000]	2700	3440	6060	300	FP
	(5000,11000]	2800	3460	6070	300	FP
	(11000,21000]	2900	3640	6370	300	FP
	(21000,31000]	3000	3980	6960	400	FP

MESH

Model Volume ($\mathrm{km} \times \mathrm{km} \times \mathrm{km}$)	**#Elements**	**Spectral Degree**	**Δt (s)**	**Duration (s)**	**Fmax (Hz)**
$82 \times 64 \times 31$	753,211	3	10^{-3}	40	1.5

REFERENCES

Publications & Reports	Smerzini.C et al. (2017). Evaluation of earthquake ground motion and site effects in the Thessaloniki urban area by 3D finite-fault numerical simulations, *Bulletin of Earthquake Engineering* **15**, 787-812
Link to Website / Repository	http://speed.mox.polimi.it/WebRepository/

GRC_1978.06.20_23.03lt_Mw6.5	
Map of Receivers	Fault Rupture Scenario
	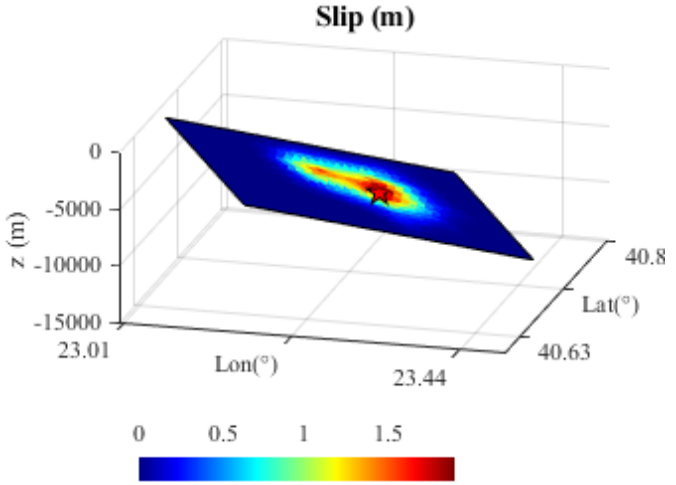
Site Proxy: Depth to bedrock (H_{bed})	Site Proxy: Equivalent Shear Wave Velocity ($V_{S,eq}$)
	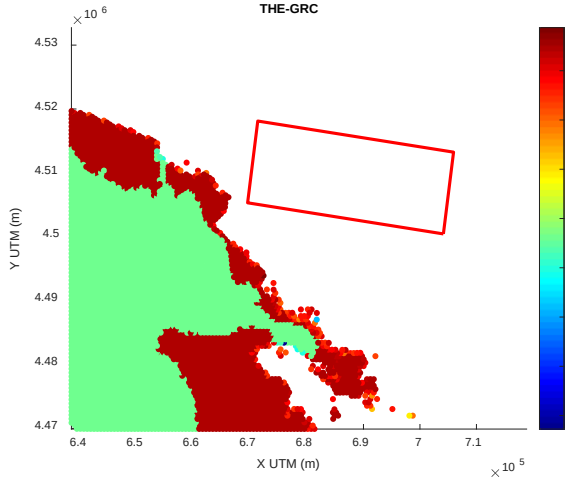

GRC_1978.06.20_23.03lt_Mw6.5

	FN Component	FP Component
PGA	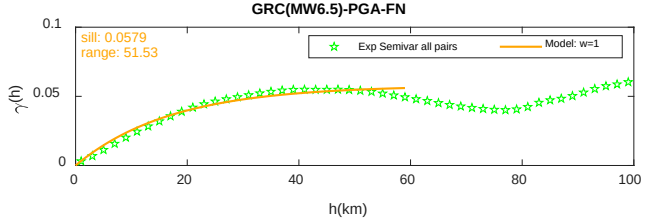	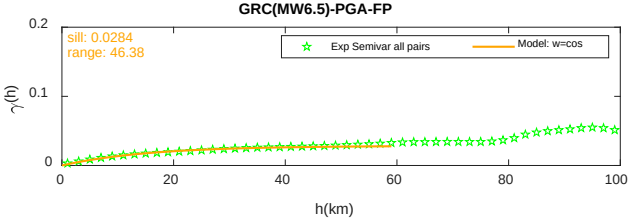
SA(1s)	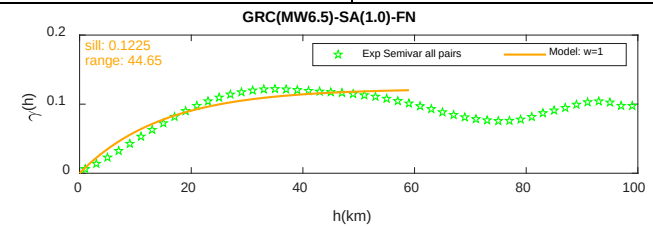	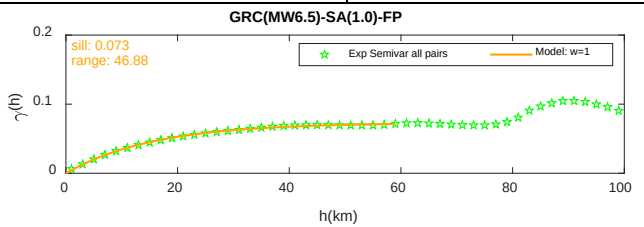

GRC_THE_ANTHEMOUNTAS_MW7.0_S001	
Map of Receivers	Fault Rupture Scenario
	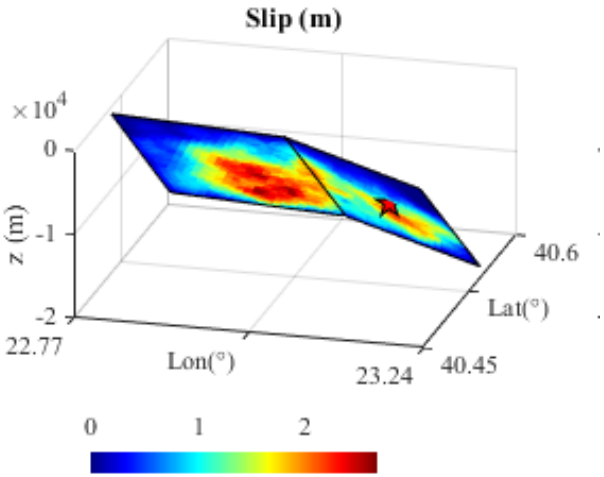
Site Proxy: Depth to bedrock (H_{bed})	Site Proxy: Equivalent Shear Wave Velocity ($V_{S,eq}$)
	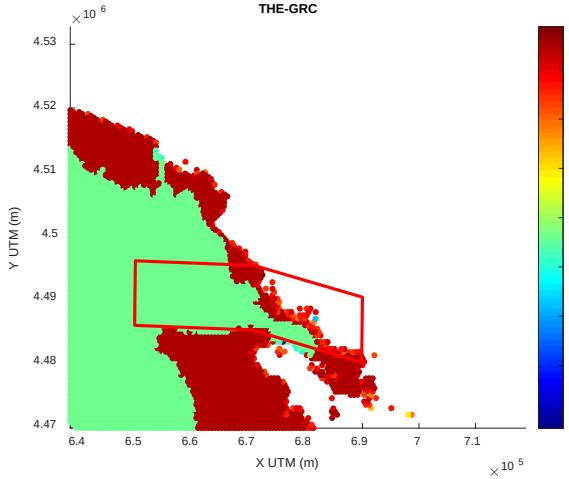

GRC_THE_ANTHEMOUNTAS_MW7.0_S001

	EW Component	NS Component
PGA	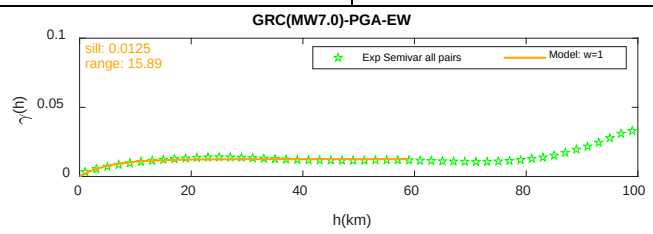	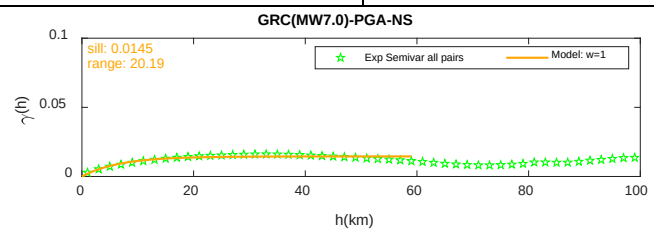
SA(1s)	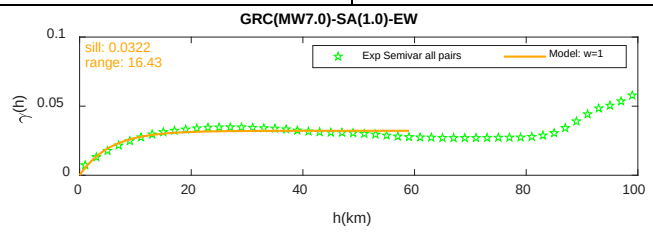	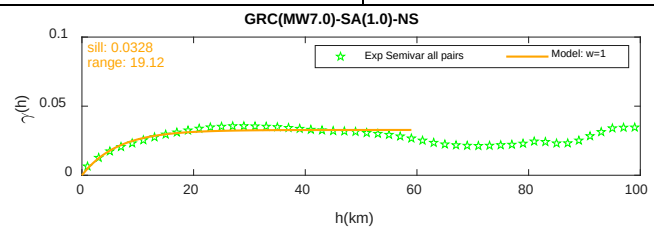

TUR_IST		
COUNTRY	**LOCATION**	**FAULT**
IST	TURKEY	NORTH ANATOLIAN

VELOCITY MODEL

(1) BASIN / SUPERFICAL MODEL

Depth z (m)	**V_S (m/s)**[(i)]	**V_p (m/s)**[(ii)]	**Q_s(-)** [(iii)]	**Damping Type**[(iv)]	**Soil** [(v)]
[0,2000]	c_1=250, c_2=1, c_3=0.50	R_{PS} = 1.6	Q_0 = $V_s(z)/10$ F_0=1	FP	LVE
[2000,5000]	Linear increase	R_{PS} = 1.6	Q_0 = $V_s(z)/10$ F_0=1	FP	LVE

(i) $V_S = c_1 + c_2 \cdot z^{c3}$

(ii) $V_p(z) = R_{pS} \cdot V_S(z)$

(iii) $Q_S = (Q_o \cdot f)/f_o$, f is the frequency in Hz

(iv) FP: frequency proportional

(v) LVE: Linear visco-elastic

(2)CRUSTAL MODEL

Depth z(m)	**V_S (m/s)**	**V_p (m/s)**	**Q_s (-)**	**Damping Type**
(5000,10000]	3490	5770	350	FP
(10000,20000]	3500	6390	350	FP
(20000,30000]	3920	6790	400	FP

MESH

Model Volume ($\mathrm{km} \times \mathrm{km} \times \mathrm{km}$)	**#Elements**	**Spectral Degree**	**Δt (s)**	**Duration (s)**	**Fmax (Hz)**
$165 \times 100 \times 30$	2,257,482	4	10^{-3}	60	1

REFERENCES

Publications & Reports	Infantino, M. et al. (2020). 3D physics-based numerical simulations of ground motion in Istanbul from earthquakes along the Marmara segment of the North Anatolian Fault, *Bulletin of the Seismological Society of America* **110(5),** 2559-2576
Link to Website / Repository	http://speed.mox.polimi.it/WebRepository/

TUR_IST_NAF-CMS-PIS_MW7.0_S001/S0020/S0023/S0025	
Map of Receivers	Site Proxy: Equivalent Shear Wave Velocity ($V_{S,eq}$)
	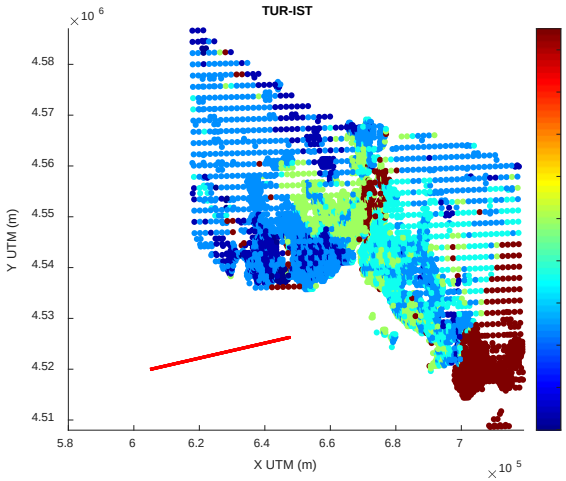
Slip distributions	
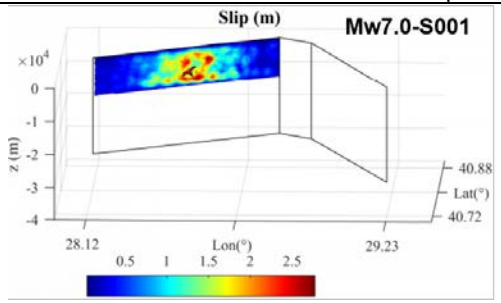 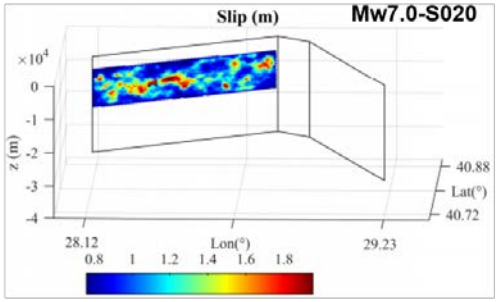 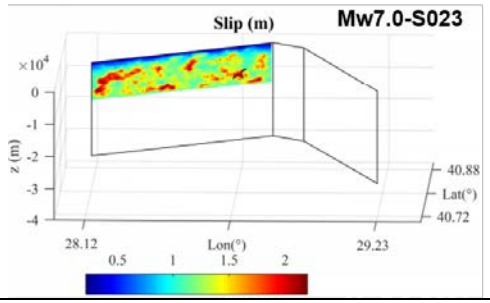 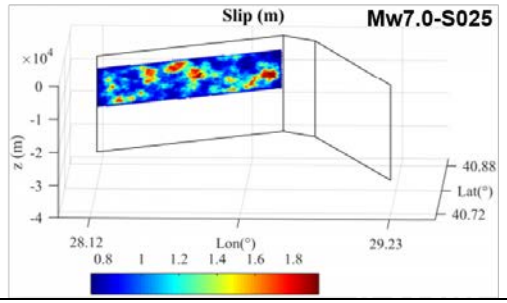	

TUR_IST_NAF-CMS-PIS_MW7.0_S001

	EW Component	NS Component
PGA	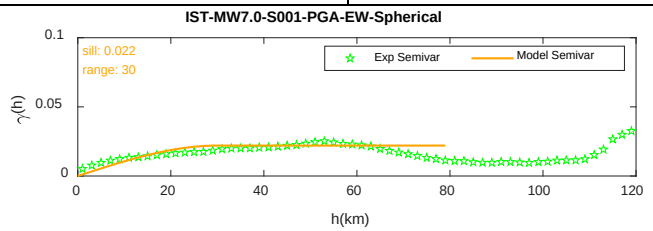	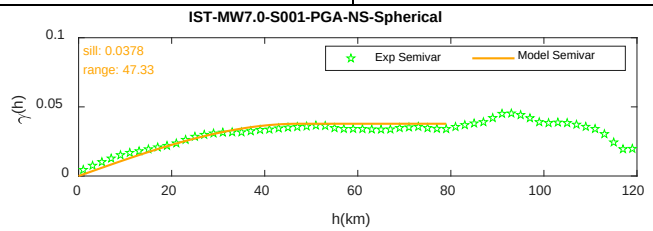
SA(1s)	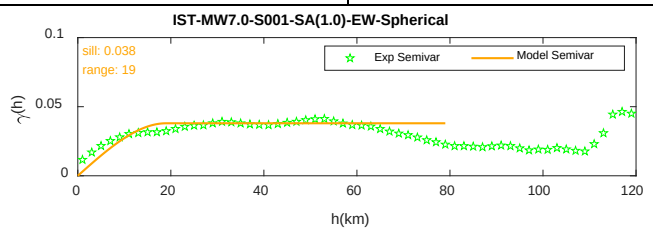	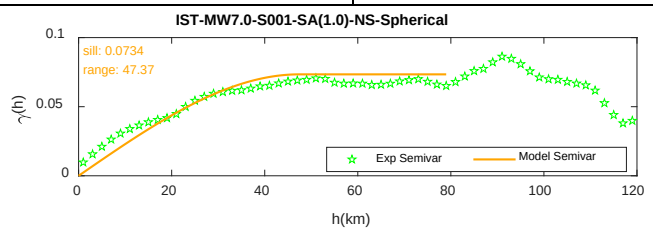

TUR_IST_NAF-CMS-PIS_MW7.0_S020

	EW Component	NS Component
PGA	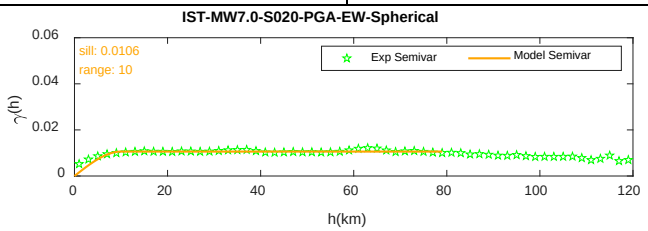	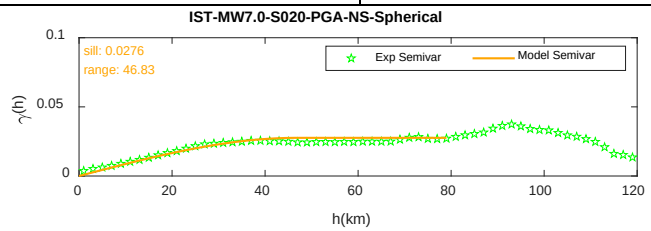
SA(1s)	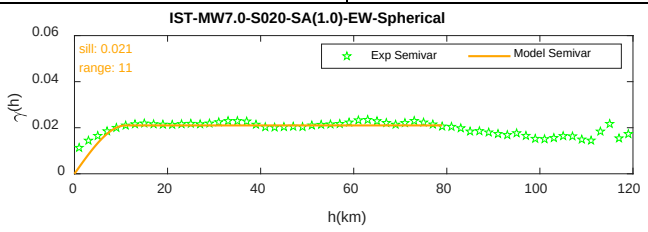	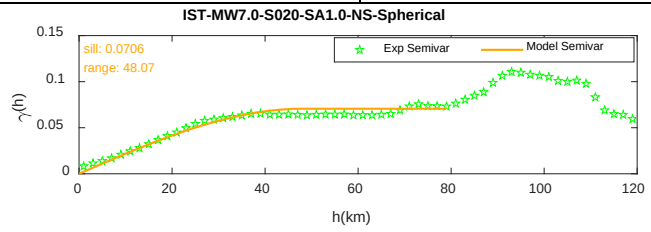

TUR_IST_NAF-CMS-PIS_MW7.0_S023

	EW Component	NS Component
PGA	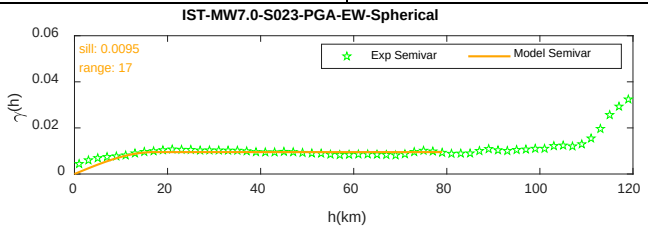	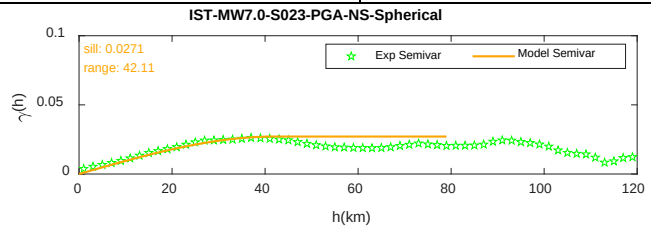
SA(1s)	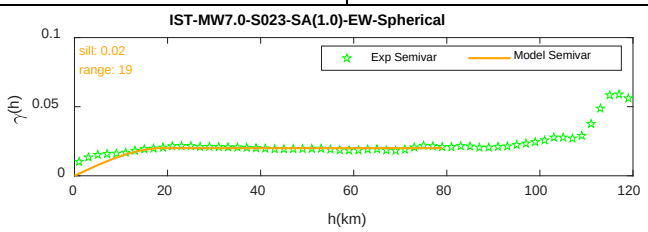	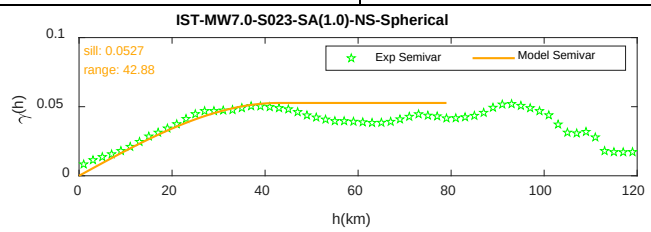

TUR_IST_NAF-CMS-PIS_MW7.0_S025

	EW Component	NS Component
PGA	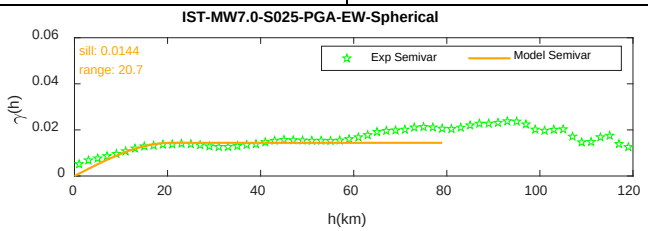	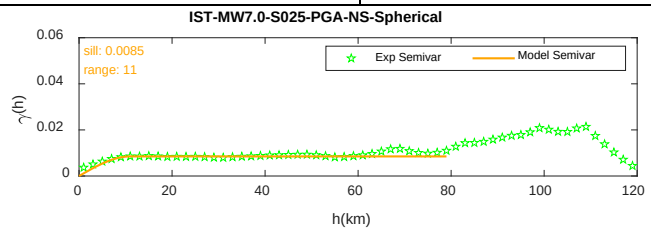
SA(1s)	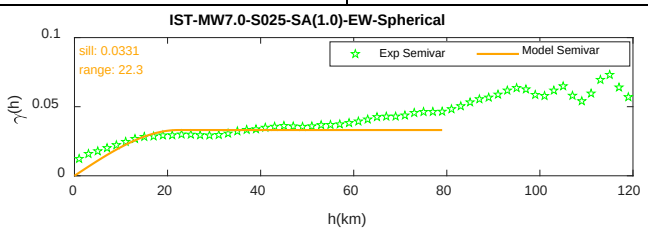	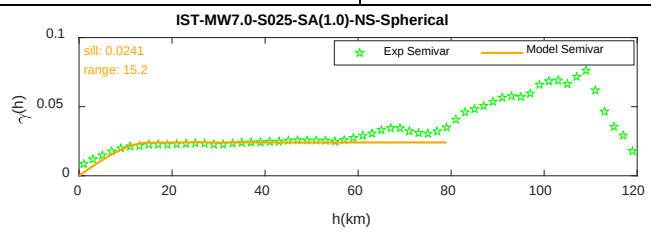

TUR_IST_NAF-CMS-PIS_MW7.4_S001	
Map of Receivers(e.g. MW7.0_S001)	Site Proxy: Equivalent Shear Wave Velocity (VS,eq)
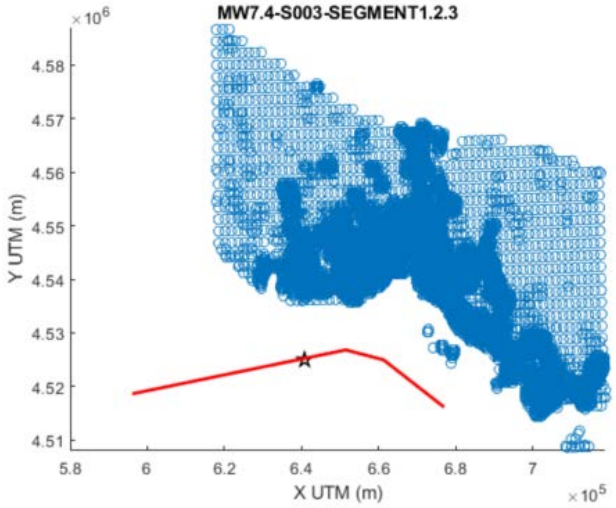	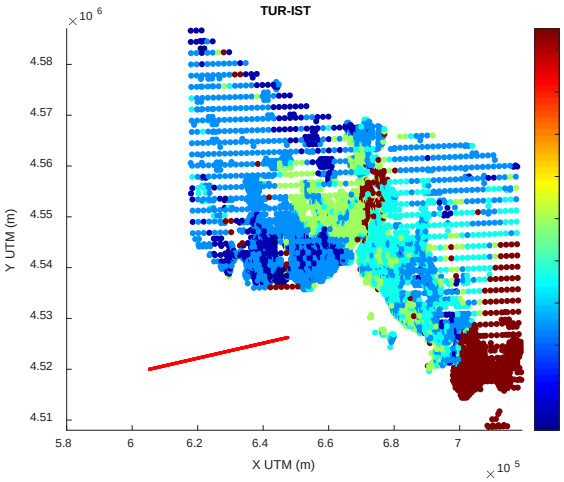
Slip distribution: MW7.4_S001	
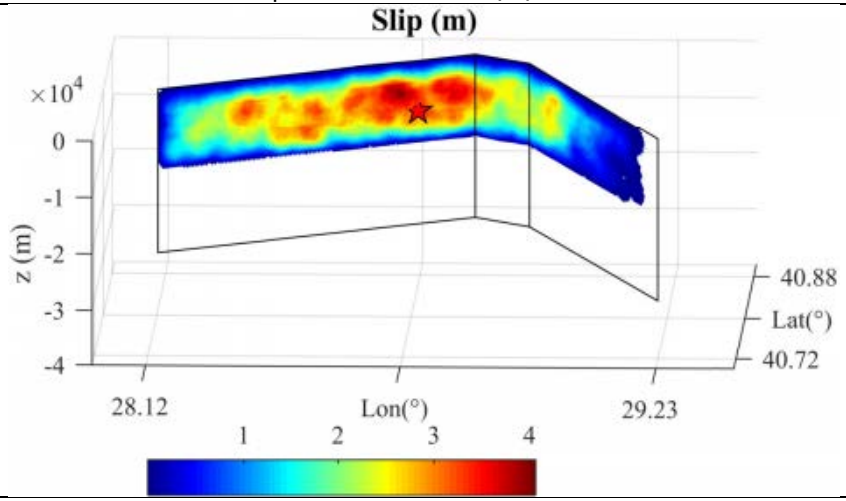	

TUR_IST_NAF-CMS-PIS_MW7.4_S001

	EW Component	NS Component
PGA	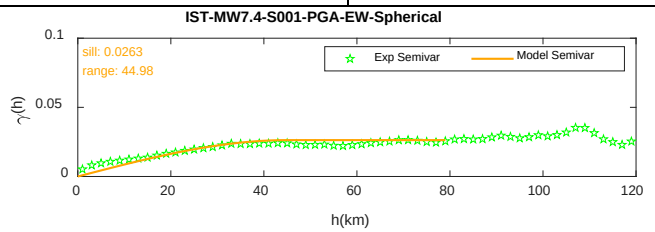	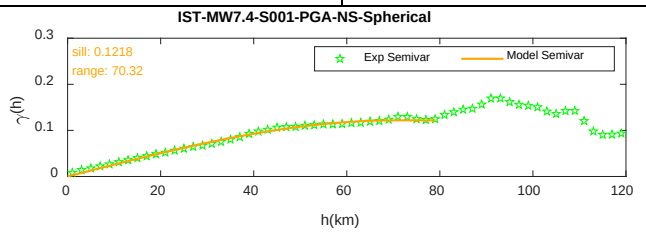
SA(1s)